

**TRIBOELECTRICITY AND PIEZOELECTRICITY BASED 3D PRINTED  
BIO-SKIN SENSOR FOR CAPTURING SUBTLE HUMAN MOVEMENTS**

by  
**Mo Lv**

**A Thesis**

*Submitted to the Faculty of Purdue University  
In Partial Fulfillment of the Requirements for the degree of*

**Master of Science in Industrial Engineering**



School of Industrial Engineering

West Lafayette, Indiana

May 2019

**THE PURDUE UNIVERSITY GRADUATE SCHOOL  
STATEMENT OF COMMITTEE APPROVAL**

Dr. Wenzhuo Wu, Chair

School of Industrial Engineering

Dr. Denny Yu

School of Industrial Engineering

Dr. Brandon Pitts

School of Industrial Engineering

**Approved by:**

Dr. Steven Landry

Head of the Graduate Program

## TABLE OF CONTENTS

LIST OF FIGURES .....	4
ABSTRACT.....	6
CHAPTER 1. INTRODUCTION.....	8
1.1 Background and Problem Definition .....	8
1.2 Literature Review.....	8
1.3 Scope of the Research.....	10
1.4 Use of Material .....	10
1.5 Use of Software and Equipment .....	11
CHAPTER 2. EXPERIEMENT AND METHODOLOGY .....	13
2.1 Design Concept for 3D Printing .....	13
2.2 Material Preparation.....	14
2.3 3D printing of the Bio-skin.....	15
2.4 Electrical Characterization.....	19
CHAPTER 3. RESULTS AND DISCUSSION .....	21
3.1 Advantages of Wearable Device Fabrication with 3D Printing.....	21
3.2 Operating Mechanism of the Bio-skin.....	22
3.3 Results from TE Bio-skin Optimization Process .....	26
3.4 Electrical Characterization of the Bio-skin.....	30
CHAPTER 4. DEMONSTRAION.....	35
4.1 Heart Pulse Rate Measurement and Health Monitoring .....	35
4.2 Detection on Human Acoustic Waves .....	40
4.3 Detection on Large Degree of Body Movements .....	43
CHAPTER 5. CONCLUSIONS AND RECOMMENDATIONS .....	45
5.1 Conclusions.....	45
5.2 Study Gap and Recommendations .....	46
REFERENCES .....	53

## LIST OF FIGURES

<b>Figure 1.</b> CAD Design of the Initial TE Bio-skin and its Section View.....	13
<b>Figure 2.</b> CAD Design of the PE Bio-skin with Sierpinski, Hilbert, and Peano Structure .....	14
<b>Figure 3.</b> Printing Steps and Results of the Unoptimized TE Bio-skin .....	16
<b>Figure 4.</b> Printing Steps and Results of PE Bio-skin(s) .....	18
<b>Figure 5.</b> 5 TE Bio-skin Structures. Left to Right: Circle, Mesh, Wave, Honeycomb and Solid film .....	19
<b>Figure 6.</b> 6 Circle Structure of 6 Thicknesses ( $\mu\text{m}$ ). Left to Right: 200, 400, 600, 800, 1200, 1600 .....	19
<b>Figure 7.</b> Experiment Setup for Electrical Measurements under Two Modes.....	20
<b>Figure 8.</b> Illustration of the Alignment of Te NWs in PDMS, Inset is the Optical Image .....	22
<b>Figure 9.</b> The operating mechanism of the TE Bio-skin.....	24
<b>Figure 10.</b> The operating mechanism of the PE Bio-skin .....	26
<b>Figure 11.</b> Tensile Comparison from Experiment and FEA Simulation with hyperelastic material (Right) of 5 structures .....	27
<b>Figure 12.</b> Tensile Comparison from circle structure of 6 thicknesses.....	28
<b>Figure 13.</b> Samples Printed with/without Water in PDMS Mixture and Tensile Comparison.....	29
<b>Figure 14.</b> Optimized TE Bio-skin and Tensile Comparison with Unoptimized TE Bio-skin.....	30
<b>Figure 15.</b> $I_{sc}$ , $V_{oc}$ , $Q_{sc}$ of the Unstretched TE Bio-skin and its Output Power with Varying Resistance of External Loads.....	31
<b>Figure 16.</b> Electrical Durability Test and Dual Modes Test of the TE Bio-skin .....	32
<b>Figure 17.</b> $I_{sc}$ , $V_{oc}$ of the PE Bio-skin(s) and Without Te NWs .....	34
<b>Figure 18.</b> Electrical Power, Strain-responsive Signals, and Durability Test of the Peano PE Bio-skin.....	34
<b>Figure 19.</b> Heart Pulse Rate Measurement on Neck and Wrist with TE Bio-skin.....	36
<b>Figure 20.</b> One Period Cycle of Heart Pulse rate Measured from Neck and Wrist with TE Bio-skin .....	37
<b>Figure 21.</b> Heart Pulse Rate Measurement on Neck and Wrist with PE Bio-skin.....	39
<b>Figure 22.</b> One Period Cycle of Heart Pulse rate Measured from Neck and Wrist with PE Bio-skin .....	40

<b>Figure 23.</b> Speech Recognition with FFT analysis of the 3 words ('Purdue', 'Boiler', 'up') .....	41
<b>Figure 24.</b> Average Wavefunction and Voice Spectrogram .....	42
<b>Figure 25.</b> Average Wavefunction with FFT analysis of the 3 words ('Purdue', 'Giant', 'Leaps') and Voice Spectrogram.....	43
<b>Figure 26.</b> Detection of Different Bending angles from the Participant's Elbow.....	44

## ABSTRACT

Author: Lv, Mo. MS

Institution: Purdue University

Degree Received: May 2019

Title: Triboelectricity and Piezoelectricity Based 3D Printed Bio-skin Sensor for Capturing Human Movements

Committee Chair: Wenzhuo Wu

**Bio:** Mo Lv is a Master of Science graduate student in Industrial Engineering at Purdue University, with a specialization in the field of Manufacturing. His research focus is on 3D printing of responsive wearable electrical devices with hydrogels and Nano-materials.

**Abstract:** The first phase of the research presents a novel flexible electrical sensor device, namely 3D printed triboelectric (TE) bio-skin, designed and fabricated with the additive manufacturing technique. Negative-charging material Polydimethylsiloxane (PDMS) matrix is selected as the dielectric layer of the device with fluidic electrode carbon grease embedded. Triboelectric effect and electrical induction are exploited for sensing subtle movements such as heart pulse, human acoustic sound waves, and large human joints movements. Prior to the make of electrical devices using traditional fabrication methods, such 3D printed TE bio-skin has a controllable design and thickness depending on the requirements from the user.

We also conducted tensile test experiments on the optimization process of the TE bio-skin to select the proper design and thickness for the improvements on its mechanical performance. The final shape of the device is designed with circle structure to be more air-permissible and presenting a robust mechanical property by reaching an average maximum strain of 151.67% and a lateral Force-Displacement of 0.21N/mm, with mechanical performance greatly enhanced, compared with the results maximum strain of 47.33%, lateral Force-Displacement of 0.37N/mm before optimized. It also possesses the triboelectric property with an average output voltage of 6V, short circuit current of 14nA, and transferring charge of 2nC through oscillatory touch between the device and another type of positive material, such as medical plastic tape in this research. The

optimized device has a resistance-dependent output current, and able to reach a maximum power of  $36.36nW$  at  $600M\Omega$ . Through triboelectric effect, it is also proven to function under contact or stretching mode.

The second phase focuses on utilizing piezoelectric polarization for the make of bio-skin devices through inkjet 3D printing. For the Piezoelectric (PE) bio-skin, Te-PDMS was used as the printing piezoelectric material by mixing synthesized Te NWs with PDMS matrix, in which the piezoelectric Te NWs were believed to be able to align perfectly along the printing path for an enhanced electrical output. PE bio-skin devices in 3 fractal structures (Peano, Hilbert, Sierpinski) are electrically compared and the Peano PE bio-skin exhibits the largest output current  $6.15nA$  and voltage  $2.85V$ . The Peano PE bio-skin is also proven to be signal-responsive with the stretching strain and can reach a maximum power of  $11.32nW$  at  $400M\Omega$ .

Both optimized TE bio-skin and PE bio-skin are tested to be electrically stable as well. This work demonstrates with such devices to effectively detect human's health status by monitoring the heart pulse rate on the neck and wrist respectively in real-time, and identifying human speech patterns through collecting signals measured from vibrations of the human voice cord. Additionally, the TE bio-skin is also demonstrated to utilize its proven stretchability to detect large movements from the human body.

## CHAPTER 1. INTRODUCTION

### 1.1 Background and Problem Definition

Mechanical energy can be stored in many ambient environments, such as wind, water waves, sound waves, etc. [1,2,3]. To harvest these enormous energies, emerging technology nowadays has been developed with various methods, such as building dams, wind turbines, or other large facilities. Most mechanical energy can be transformed into electricity or other forms of energy which are beneficial for people in their daily use, and the mechanical energy conversion efficiency is likely to continue the increase with other novel methods introduced. However, there are other potential mechanical energy resources existing in imperceptible movements that are usually wasted, such as human motions, joint movements, or vibration from voice band, etc. [4].

### 1.2 Literature Review

In the past few years, researchers found interest in the development of low-cost, self-powered, and efficient energy-scavenging devices, such as triboelectric nanogenerators (TENGs) and piezoelectric nanogenerators (PENGs), to harvest such small mechanical energy for powering source or sensing purpose [5,6,7,8,9,10]. Both TENGs and PENGs show their promising applications in sustainable power source supplying [2,7,8], self-powered sensing [11], position mapping [12], etc. Typically, wearable flexible electrical sensors have attracted many attentions in the development of material selection, structural design, and fabrication techniques. Traditional flexible electrical devices can be created in an effective and accurate manner with the methods such as coating [13], molding [14,15], physical or chemical vapor deposition [15], screen printing [16], knitting [17,18], etc. but there also exists a certain gap that limits their applicability between laboratory research and industry manufacturing. Other shortcomings in device making such as high cost, complex procedures, or stringent requirements for the setup, can also prevent their potential development in the future.

With the introduction of self-powered PENGs that can transform mechanical energy into electrical energy through the piezoelectrical polarization process, the 1-dimensional nanowires (NWs) in

micro/nano scale have been largely studied due to their high ratio of surface area and volume, and distinguished mechanical/electrical properties that are superior than their counterparts in bulk phase [19]. To list some, wurtzite materials such as ZnO, GaN, CdS, etc. [20, 21], perovskite materials [22, 23], are the main piezoelectric materials with the high convergency rate. The PENG device with piezoelectric semiconductors such as Tellurium (Te) is utilizing the coupling of piezoelectricity and semiconductor property. Te element in the asymmetric crystalline structure has been reported to have many applications in the making of electrical device due to its shorter band-gap energy at room temperature [24], such as high piezoelectric or thermal sensor, gas sensor, optical response device, etc [25, 26]. We believe that Te NWs could be the ideal material for a typical piezoelectric device. However, only Te NWs with orientation fixed can be fully taken advantage for the formation of piezoelectric polarization as reported [27, 28]. Moreover, other obstacles such as complex fabrication methods, weak performance in small scale, wearability of the device with Te-NWs, etc. can also be a major concern for the Te-PENGs.

Addictive manufacturing, which is known as 3D printing technique, has been widely used in recent years and focused by many researchers to assist in making electrical devices [29,30,31,32]. 3D printing technique utilizes the rapid prototyping process to fabricate physical models from a 3D digital design via successive layers patterning [33,34], and it saves additional need for other manufacturing process such as mask, milling, or molding. Complex components structure can be directly translated into a precise physical entity via printing in a faster manner, also preventing unnecessary waste of the material used, compared with the conventional methods. Thus, 3D printing technique can potentially enhance the fabrication process of small energy harvesting devices by improving the mechanical performance with its controllability on the design of the device. 3D printing has been applied on multiple manufacturing or research fields [35]. To highlight some, soft implanted medical devices [36], soft robot components [32, 37], wearable electrical sensors [29, 38,39], etc. are fabricated in a friendly way for humans to be able to interact with.

### 1.3 Scope of the Research

In the first phase of this study, we report a novel electrical sensor device, namely 3D printed Triboelectric (TE) bio-skin with mesh structure, utilizing the principle of triboelectrification through generated charge from the contact and separation between two materials of opposite polar. Such electrical device has utilized the inkjet printing technique, which is a liquid-based material deposition technique that involves the ejection of ink onto the substrate through a nozzle, in result of meeting both functionality and design requirements for the electrical device. Computer-Aid Design (CAD) provides free design of the device geometry in a fast and customized way. A series of mechanical property investigations are studied through the tensile test to maximize its physical performance. The mechanical and electrical functionality of the final device are characterized in this report. The optimized 3D printed TE bio-skin will also be demonstrated to monitor human health through testing the heart pulse rate from a human body on the wrist and neck respectively, and human health status can be analyzed from the data collected by the TE bio-skin [37, 38]. The speech pattern is also demonstrated by collecting the electrical signals measured from the human voice cord. To demonstrate the enhanced mechanical performance and ability of mechanical energy harvesting, the device will be attached to human elbow to detect large joint movements. In the second phase, we developed a 3D printed Te-PENG bio-skin device, namely piezoelectric (PE) bio-skin, which is composed of Te NWs to utilize the piezoelectric polarization principle for scavenging subtle mechanical energy. 3 fractal structures are designed and electrically compared and characterized. The demonstration is similar to the TE bio-skin from the 1<sup>st</sup> phase of study on human pulse detection and speech recognition.

### 1.4 Use of Material

The structure of the TE bio-skin is composed of single fluidic electrode, which is embedded within a type of stable and stretchable material, Polydimethylsiloxane (PDMS) in this study. PDMS matrix has been largely used on medical research [40,41,42], electrical device fabrication [8,43], 3D bioprinting [42], etc. due to its robust mechanical and electrical properties [43,44], and bio-compatibility with the human skin. [45,46] Viscoelastic PDMS in hydrogel state mixed with curing agent has been reported to be printable through deposition nozzles in 3D printing. Such mixture can transform into a stable elastomer at a low glass transition temperature or under UV light. It is

showcased that PDMS shall retain its shape during the printing and curing process, and can be a promising candidate for the dielectric layer in the 3D printed TE bio-skin due to its negative electrical property aspect. Printable conductive carbon grease does not dissociate or react with PDMS and is able to elongate or deform with PDMS without break due to its rheological property. Both materials are at low cost, chemical inert with each other, and bio-compatible to human bodies. For the PE bio-skin, besides PDMS and carbon grease, ultrathin Te NWs in asymmetric structure are also used to generate piezoelectric potential for the device through dislocation of the positive Te ions and the negative charge center against the cores of Te. The detailed crystal structure and working mechanism of Te NWs will be discussed in Chapter 3. Ecoflex is also used as the printing substrate and sealing materials for the PE bio-skin.

### 1.5 Use of Software and Equipment

Below are the lists of software and equipment used in the research study:

#### **Software:**

1. SolidWorks – CAD software mainly used for the design and conversion of the 3D modeling into STL (stereolithography) file format, which is readable for the software used in 3D printing.
2. Slic3r – Open source software to splice the 3D model into countable layers by generating G-codes (A widely used programming language for computer numerical control machines) from STL file. The G-code is editable and readable commands for the 3D printer.
3. Repetier-Host – Application software used for interacting with the 3D printer, such as printing calibration, sending G-codes, controlling printing speed, etc.
4. ANSYS Workbench – Environmental analysis software used for the tensile simulation of the 3D models.
5. OriginPro – Application software used for data analysis and graphic plotting in this research.
6. MATLAB – Application software for calculating Fast Fourier Transform with built-in algorithm and plotting spectrogram graphs.

**Equipment:**

1. The CELLINK INKREDIBLE 3D Bioprinter – The bio-printer used for printing viscous cells, bio-materials, hydrogels or liquid-like materials. PDMS and carbon grease are printable with the printer.
2. MTS 810 – The Mechanical testing machine system used for characterizing the tensile properties of the printing samples in the research with controllable tensile speed and load unit.
3. LinMot – The motorized linear translation stage used for applying x-axis periodical contact to the test device in electrical and mechanical characterization.
4. SR570 – The low-noise current preamplifier used to measure the short-circuit current ( $I_{sc}$ ).
5. Keithley Model 6514 – The electrometer used to measure open-circuit voltage ( $V_{oc}$ ) and short-circuit transferring charge ( $Q_{sc}$ ).

## CHAPTER 2. EXPERIEMENT AND METHODOLOGY

### 2.1 Design Concept for 3D Printing

#### (A) TE Bio-skin

SolidWorks CAD software was exploited to make the design of the initial TE bio-skin. Figure 1 shows the design concept of the TE bio-skin. The base part of the device (unoptimized TE bio-skin in Figure 1) was designed as mesh structure with a line intersecting pattern, and dense small hemispheres ( $r=0.8mm$ ) were attached to the surface of the base structure. The dimension of the device was set as  $50mm \times 10mm \times 1.6mm$  excluding the hemispheres on top. It is noticed that the device was composed of two types of materials in a multi-layer embedded structure manner. PDMS matrix mixed with curing agent was selected for the white section in CAD design. The cross-sectional area indicates that a thin layer of second type of material, which is carbon grease (black color), of the same design of the base part was made inside. The 3D model was exported in STL file format for the printing process.

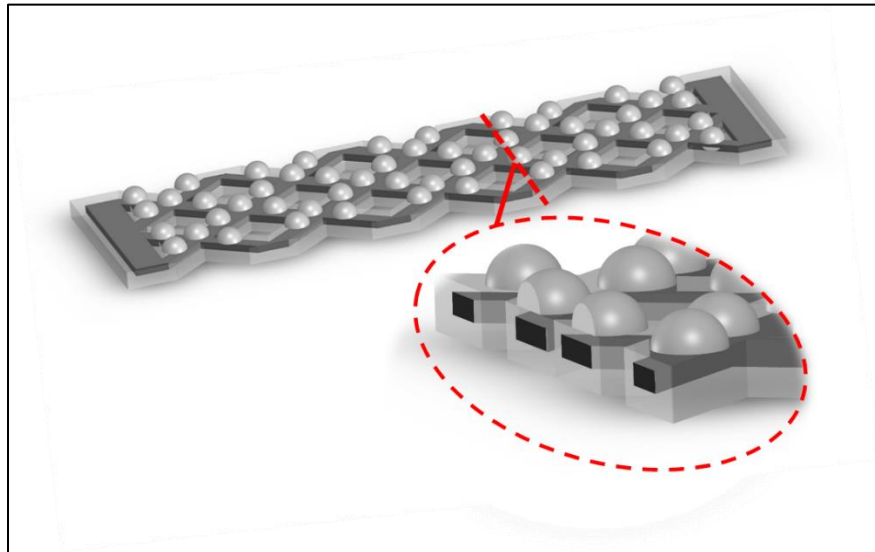


**Figure 1a.** CAD Design of the Initial TE Bio-skin and its Section View.

## (B) PE Bio-skin

The 3D printed PE bio-skin model was also designed with SolidWorks CAD software. 3 fractal structures that are formed by winding of the lines were designed based on the shape reported [47]. Figure 2 schematically illustrates the 3 proposed structures [47] of PENGs, namely Sierpinski (left), Hilbert (upper right), and Peano (lower right) respectively. Hilbert structure PE bio-skin was designed with a planer dimension of  $43\text{mm} \times 43\text{mm}$ ; Peano structure's dimension was  $40\text{mm} \times 40\text{mm}$  and Sierpinski structure's dimension was  $33\text{mm} \times 33\text{mm}$ . The cross section of the line unit was  $0.6\text{mm} \times 0.8\text{mm}$  ( $W \times H$ ). The Te-PDMS in silver-gray color, which is the mixture of Te NWs and PDMS matrix with a weight ratio of 1:100, is sandwiched between the electrodes printed with carbon grease placed on the top and bottom.

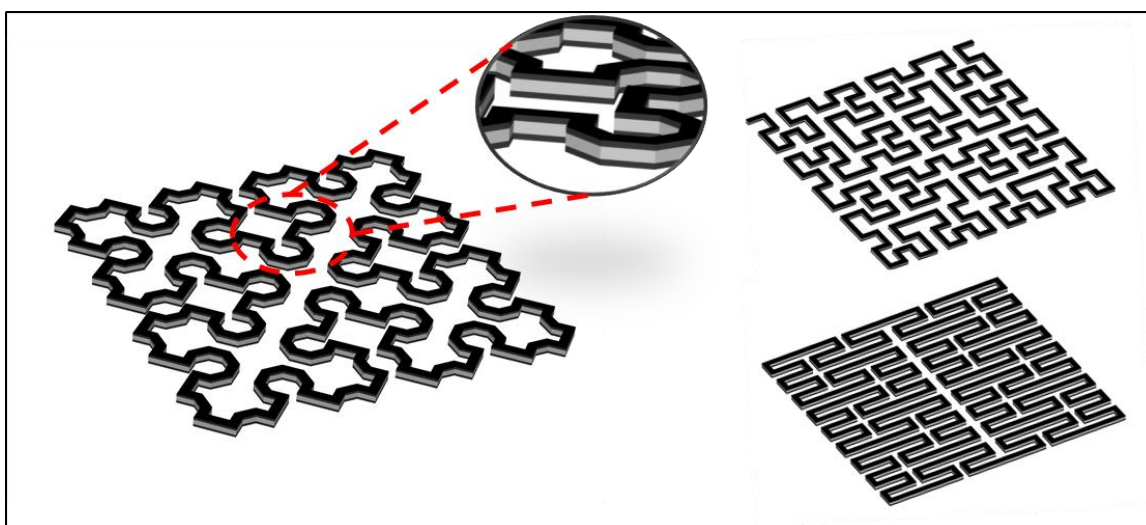


**Figure 2.** CAD Design of the PE Bio-skin with Sierpinski, Hilbert, and Peano Structure

## 2.2 Material Preparation

## (A) PE Bio-skin

Hydrogel PDMS mixture was prepared by mixing 5g highly viscous PDMS adhesive matrix (Sylgard 184, Dow Corning), 0.5g curing agent (attached with PDMS) and 1g distilled water. The mixture was stirred for 5 mins with a glass rod until the color tends to be opaque white. PDMS matrix hydrogel mixture was transferred to the printing Extruder 1 for making the dielectric layer and small hemispheres of the device. 5g Carbon grease (#846-1P, MG Chemicals) was uniformly

mixed for 5 mins, and was placed into Extruder 2 for printing the fluidic electrode layer (embedded part). Both printing Extruder 1 and Extruder 2 were centrifuged for 5 mins at 1500rpm to evacuate the air bubbles.

#### (B) PE Bio-skin

Besides the preparation of PDMS and carbon grease, Te-PDMS mixture were prepared by synthesizing Te NWs to uniformly mix with PDMS. 0.0922g (0.416mmol) of sodium tellurite ( $Na_2TeO_3$ , Alfa Aesar) and 1g of Polyvinylpyrrolidone ( $(C_6H_9NO)_n$ ), Alfa Aesar) were added into a Teflon vessel with 33ml double distilled water added. The mixture was uniformly mixed with a magnetic stirring rod under room temperature at 650rpm for 5mins. The powers shall fully dissolve in the clear solution. Then 1.65ml of hydrazine monohydrate (79%, TCI America) and 3.65ml of ammonium hydroxide (28-30%, BDH, ACS grade) were added to the solution. Next, the vessel was placed in the Teflon-lined stainless-steel autoclave with cover tightly closed, and heated in the oven at 180°C for 4 hours. The autoclave was cooled down at room temperature after the heating. The final solution was poured out of the vessel into tubes with acetone solution added to precipitate the solid silver-gray products. The products are centrifuged at 6,500rpm for 5 mins to remove remaining ions and then washed with water under the same centrifugation setting for additional 3 times. Similar to previous methods, the hydrogel PDMS matrix was mixed with the curing agent in a weight ratio of 10:1, Te NWs products were uniformly mixed with the PDMS for 5 minutes until the Te-PDMS mixture turns to silver-gray color.

### 2.3 3D printing of the Bio-skin

#### (A) TE Bio-skin

The nozzles with an extruding diameter of 200 $\mu$ m were installed to both printing extruders as printing heads. The printing increase height was set as 200 $\mu$ m per layer, and each layer was printed with parameter and infill. The printing speed was set as 5mm/s for parameter and 10mm/s for infill. A pressure pump was used to extrude the materials from the extruders. The pressure setting for PDMS hydrogel and carbon grease is 180MPa and 130MPa respectively depending on their viscosity property and the size of nozzle diameter. INKREDIBLE 3D Bioprinter from Cellink was used for printing the TE bio-skin. The print path was created in G-code format using an open source software named Slic3r. The software spliced the CAD mode into 3 parts vertically with a

printing density of 95%. Dual extruder mode was selected in the printing process: The bottom structure was printed with PDMS hydrogel (Extruder 1) onto PET substrate; The middle part was printed with carbon grease (Extruder 2) as infill and PDMS hydrogel as parameter; The top part including the pattern of small hemispheres was printed with hydrogel PDMS. As a result, the final composition of the printing is carbon grease embedded inside PDMS.

In the printing process of unoptimized TE bio-skin as shown in Figure 3. (1-3), PDMS and carbon grease were loaded in Extruder 1 and Extruder 2 respectively, PET was taped onto the plate as the printing substrate. Initially, Extruder 1 printed 3 layers of mesh structure with both infill pattern and perimeter, then Extruder 2 was switched to print two layers of mesh structure only with infill pattern, with the perimeters printed with Extruder 1. Subsequently, Extruder 1 printed three more layers of mesh structure with both infill pattern and perimeter to embed the carbon grease from Extruder 2 inside. Lastly, Extruder 1 printed small hemispheres that cover the top of the mesh structure. Printing demonstration can be found in A1 from the Appendix.

After printing, the sample was still attached to PET substrate as shown in Figure 3. (4), and was taken to a heating oven to be heated at 80 °C for 6 hours. After it was taken out of the oven as a cured elastomer, the PDMS became clear and sealed as shown in Figure 3. (5). A knife was used to gently remove the whole structure off from the substrate.

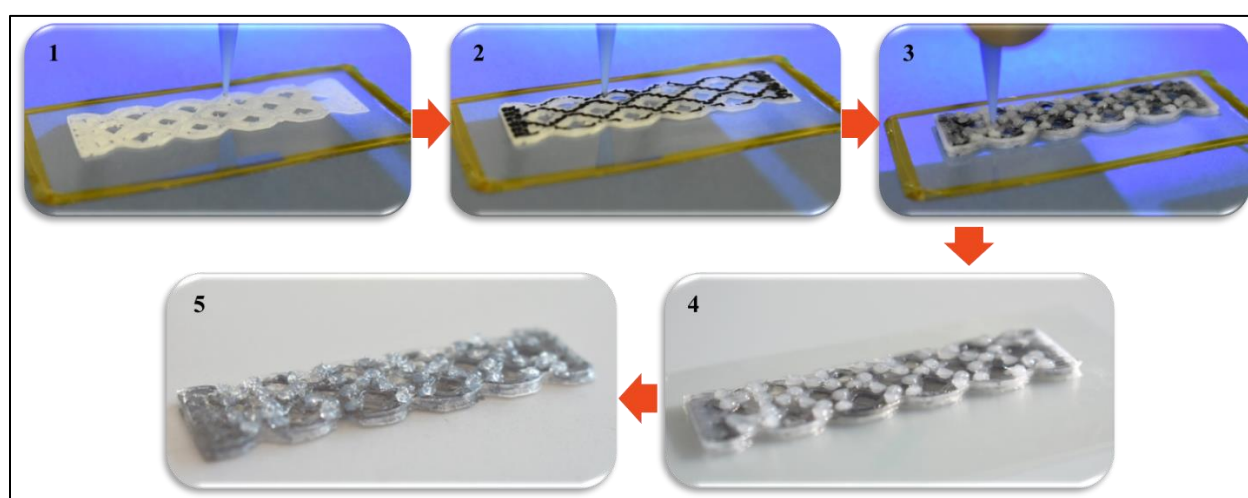


**Figure 3.** Printing Steps and Results of the Unoptimized TE Bio-skin

### (B) PE Bio-skin

Dual printing mode was still applied and the same printing nozzles were installed on the extruders. No infill pattern was generated from the G-code, and the printing speed was set at 7mm/s. Extruder 1 and Extruder 2 were filled with fluidic carbon grease and Te-PDMS mixture respectively. The ink extrusion pressure setting for the carbon grease is 130MPa; 180MPa for Te-PDMS. The printing substrate was a thin piece of clear plastic covered with a layer of Ecoflex rubber (Ecoflex 00-30) made of platinum-catalyzed silicones to hold the device. The 4-layer printing order is shown in Figure 4 as an example, in which the Sierpinski structure PE bio-skin is printed on a thin layer substrate of Ecoflex: Extruder 1 (Carbon grease) prints the 1st and 4th layers, and Extruder 2 (Te-PDMS) prints the middle two layers. Each layer was printed three times based on the structure sent to the printer (Nozzle diameter is 200 $\mu$ m; the line width is 600 $\mu$ m). When the printing is complete (3 structures as shown in Figure 4), two copper wires were placed in touch of the carbon grease from top and bottom separately. Another layer of Ecoflex rubber was poured and cured to embed the printed structure device inside. The whole device was then taken to the oven and heated at 80°C for 6 hours to cure the PE-bio-skin. After the heating, similarly, a knife was used to gently remove the device with Ecoflex off from the plastic substrate.

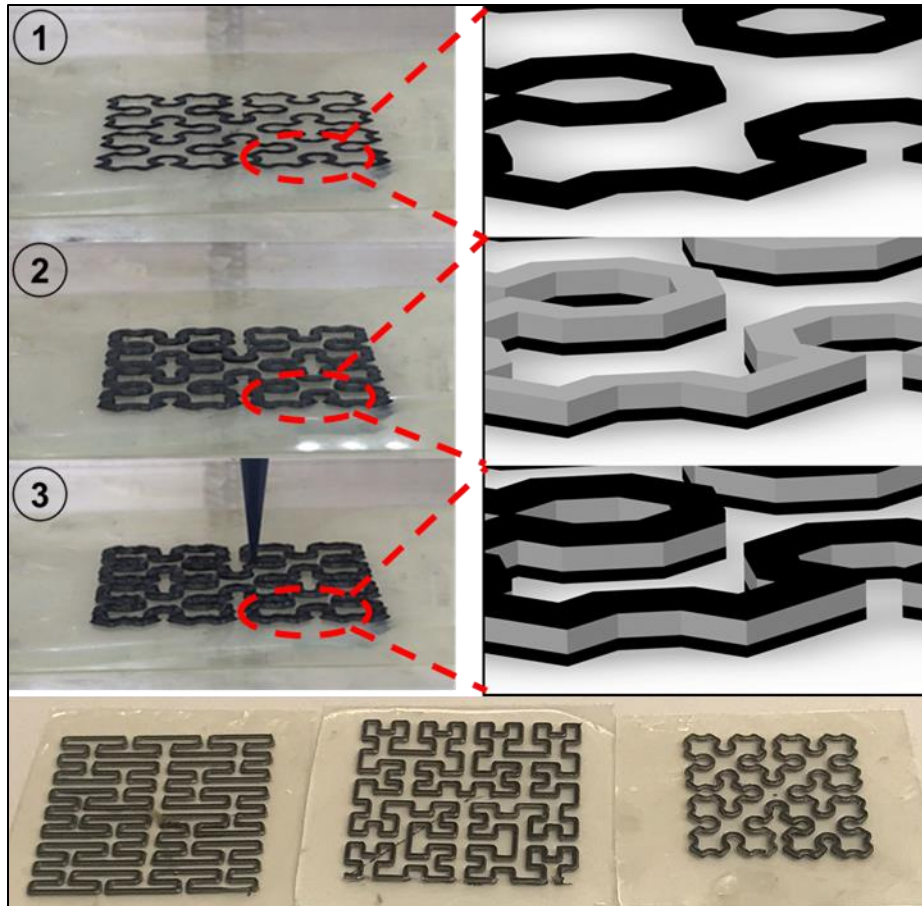


**Figure 4.** Printing Steps and Results of PE Bio-skin(s)

#### 2.4 Mechanical Optimization Process of TE Bio-skin

To investigate the optimal mechanical performance of the 3D printed TE bio-skin with the embedded structure, multi-layer printing principle. Two investigation studies on the selection of the design and thickness for TE bio-skin were conducted. To optimize the design of the TE bio-skin by reducing the elastic modulus to the minimal, 5 different structures, namely circle, mesh, wave, honeycomb, and solid film were designed and printed with the same size dimension ( $50mm \times 10mm \times 600\mu m$ ) as shown in Figure 5. Pure PDMS matrix mixed with curing agent was used for printing of the samples as it is the base material for TE bio-skin. The printing setup is the same as discussed in Chapter 2.3. 4 samples were tested for each type of the structure. Each sample was clamped tight at both ends with an effective tensile length of 30.52mm, and each sample was stretched until break with an elongation speed set at  $1mm/s$ . The results showed that circle

structure was ideal for the design of TE bio-skin (In Chapter 2.3), which is also proven from Finite Element Analysis (FEA) study of tensile test simulated with the hyperelastic material. The following investigation is to determine the optimal thickness for the device with such structure design. Figure 6 shows one sample with a thickness of  $200\ \mu\text{m}$  was breaking in the middle in tensile test, and 3D printed circle structure of 6 thicknesses ranging from  $200\ \mu\text{m}$  to  $1800\ \mu\text{m}$  by controlling countable layers (1 layer =  $200\ \mu\text{m}$ ). The preparation of samples, experiment setup and process were following the same tensile test process earlier.

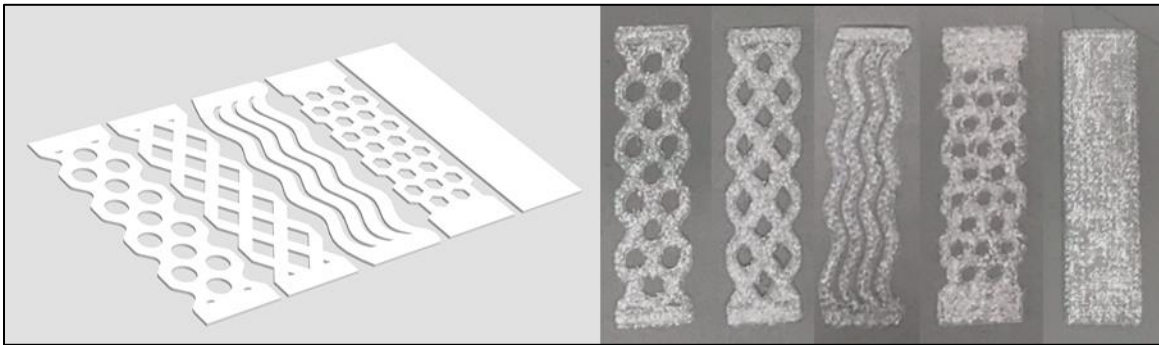


**Figure 5.** 5 TE Bio-skin Structures. Left to Right: Circle, Mesh, Wave, Honeycomb and Solid film

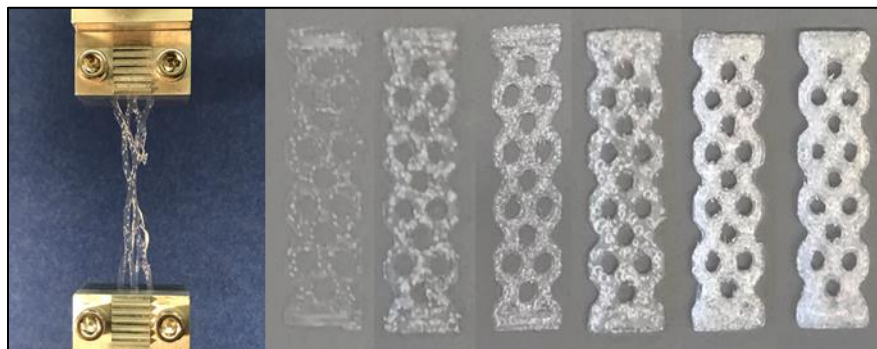


**Figure 6.** 6 Circle Structure of 6 Thicknesses ( $\mu\text{m}$ ). Left to Right: 200, 400, 600, 800, 1200, 1600

## 2.5 Electrical Characterization

To characterize the electrical outputs, the 3D printed optimized TE bio-skin was attached onto a fixed base plate which is electrical isolated. A piece of medical plastic tape was attached to the plate on the linear motor (LinMot) to periodically contact the surface of TE bio-skin, with an oscillatory frequency set to be 1 Hz. The electrometer (Keithley 6514) was used to measure voltage

$V_{oc}$ , and transferring charge  $Q_{sc}$ . A low-noise preamplifier (Stanford Research Systems, SR570) was used to measure the current  $I_{sc}$ . The electrical durability of the device was also tested by operating the linear motor for 1.1 hrs ( $\sim 2000$  cycles), and the voltage profile was collected. The output power of device was calculated from the measurements of the current and voltage of TE bio-skin with external loads of different resistance ranges from  $100M$  to  $2000M$ . Another electrical test was to determine if the  $V_{oc}$  and  $I_{sc}$  are responsive under stretching mode and contact mode, which is to simulate the two possible situations when the TE bio-skin was attached to a human body. Figure 7 shows the experiment setup: The optimized TE bio-skin was clipped tight at both ends and supported by a small piece of glass sheet. A piece of medical plastic tape was taped onto another glass sheet of same size, which was attached to a load sensor. The stretching mode was tested when a fixed pressing force 5N was applied on top of the TE bio-skin, and the TE bio-skin was stretched from 20% to 35%. In contact mode, the TE bio-skin was stretched at 10%, in contact with the pressing glass from the load unit that has an increasing force from 1N to 10N.

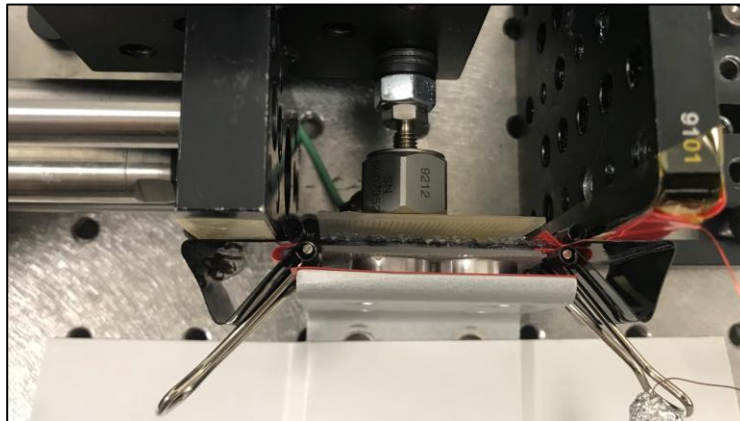


**Figure 7.** Experiment Setup for Electrical Measurements under Two Modes

## CHAPTER 3. RESULTS AND DISCUSSION

### 3.1 Advantages of Wearable Device Fabrication with 3D Printing

Prior to conventional coating method, 3D printing can provide researchers with flexibility of controlling the structure design of smart devices, and effectively meet the functionality requirements of the device. The optimized 3D printed TE bio-skin is designed with circle structure to be more stretchable and elongated with less force required than its solid structure, and such structure can also provide air-permissibility when attached to the human skin with more comfort level. The small domes patterned on the top of the base structure are designed and printed in hemisphere shape to work as spacers. Once the TE bio-skin is in contact with other materials of the opposite polar when exploiting triboelectric effect, varying contact area in pressing or releasing process can efficiently generate transferring electrical signals. With such design, both stretching mode and contact mode are compatible in the device, in assist of measuring subtle movements from human bodies or detecting large joint movements but requiring less tensile force. Traditional molding method may also be applicable for such structure, but it lacks the accuracy in the desired shape and requires additional human intervention for assembling embedded layer, multi-layer structure of multiple materials for single electrode electrical device. 3D printing with dual extruder can efficiently solves such inconvenience.

PDMS mixed with curing agent is selected to print the dielectric layer of the device structure due to its high viscoelasticity in hydrogel form before curing, and transition to rubbery state with high deformability after curing at a certain low temperature. In addition, PDMS is negative material in triboelectric series, which can be taken advantaged to apply triboelectric effect with another positive materials to generate electrical signals through contact and separation. Carbon grease is a rheological electrode material that does not dissociate PDMS, so it can be stretchable with PDMS in its optimal structure. Moreover, both materials have fine printability and can be loaded into printing extruders easily. The bio-compatible, fluidic electrode embedded multi-layer structure with enhanced mechanical improvements is ideal to be a promising electrical device for human bodies.

The PE bio-skins are designed with a fractal pattern, which describes the integrated structure that is self-similar to its repeating unit cell and across different scales. Such structure formed by a single line or loop of lines can be accommodated to various of surfaces and support many deformation modes such as biaxial, radial [47], etc. due to the enhanced elastic strain along multiple directions. The 3 fractal patterns referred in this research are suitable for the application of stretchable electrical device design such as the bio-skin concept. Another benefit of utilizing 3D printing technique is the formation of overall piezoelectrical potential. As it was mentioned earlier, the missing alignment of Te NWs could be an obstacle for the overall formation of piezoelectric potential. However, during the printing process of Te-PDMS as illustrated in Figure 8, the optical image indicates the orientation of Te-NWs mixed in PDMS can be aligned along the printing path, which is due to the shear force applied on Te NWs during the the ink-extrusion process at the nozzle, so as to ensure the formation of overall piezoelectric potential on the cross section of the PE bio-skin device.

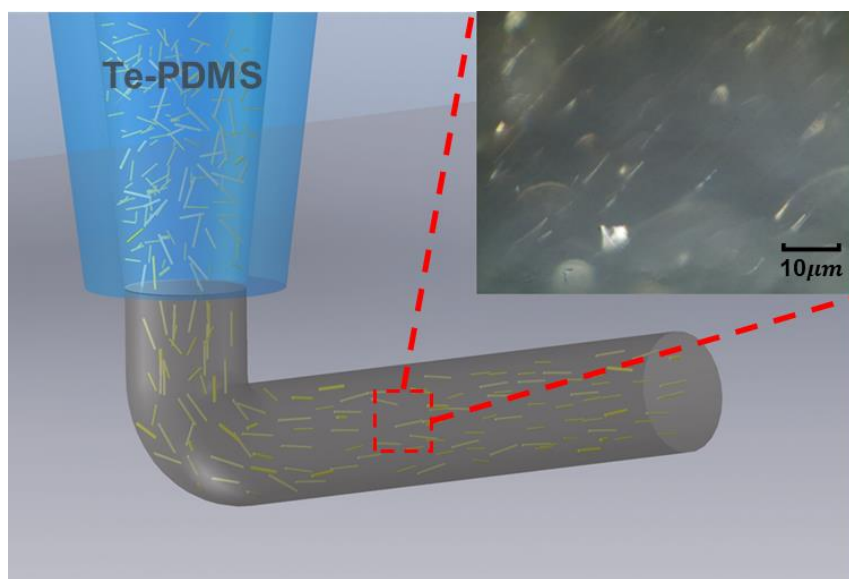


**Figure 8.** Illustration of the Alignment of Te NWs in PDMS, Inset is the Optical Image

### 3.2 Operating Mechanism of the Bio-skin

(A) TE Bio-skin

To operate the negative base material PDMS in the generation of transferring charges, a positive material, medical plastic tape in this research is chosen to be the positive material layer that is attached to the top of PDMS in its contact mode. Only non-stick side of the tape is touching the domes pattern on the top of PDMS.

The operating mechanism of 3D printed TE bio-skin is based on the coupling of electrification and electrostatic induction, which is schematically illustrated in Figure 9. Initially when there is no force applied, the surface medical plastic tape is not fully in contact with PDMS due to the spacing by small domes on PDMS, and electrical equilibrium is maintained as no electron is transferring in the copper wire (Figure 9.i). When an external force is pressed on the top (Figure 9.ii), triboelectrification, which is the generation of positive and negative electron pairs, occurs on the increasing contact area between the tape and PDMS due to their different triboelectric series from the triboelectric series chart (Appendix A2). Electrons will flow from the ground to the electrode (embedded carbon grease) through the copper wire to reach electrical equilibrium. The tape and PDMS maintains positive and negative charge respectively when the force is about to be removed, and the electrons stop moving as the ground and electrode are reaching same electrical potential (Figure 9.iii). When the force is removed, it will cause different electrical potentials between the tape and PDMS. To maintain electrical equilibrium again, the electrons will flow from the electrode to the ground due to electrostatic induction, which can cause an opposite current flow from the previous (Figure 9. iv). Ambient vibration can cause the contact and separation between the tape and PDMS, and the electrical output can help us visualize those movements in a measurable way.

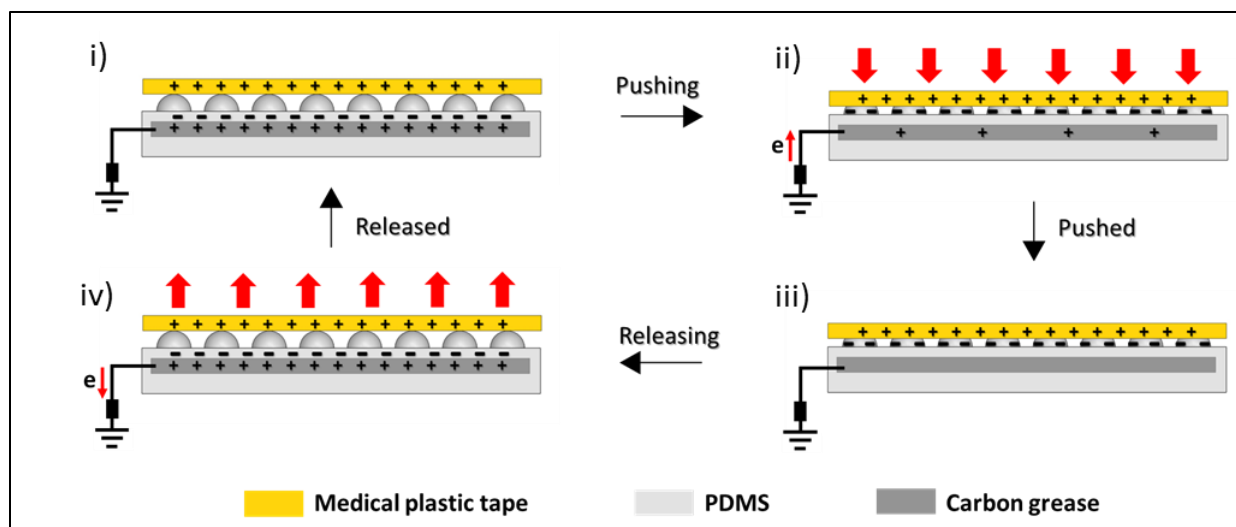


**Figure 9.** The operating mechanism of the TE Bio-skin

#### (B) PE Bio-skin

The theoretical atomic crystalline structure of Te NWs is illustrated in Figure 10.i. With the absence of the strain applied on Te NWs, the cross section of a single Te NW chain is in an equilateral triangular shape due to the helical turns of atoms with a rotating angle of  $120^\circ$  along the longitudinal direction along the NWs, which are packed by a group of Te NW chains formed in a hexagon shape in the cross-sectional view (z axis) [27, 48].

The fundamental crystal structure of Te NWs in their cross section and proposed working mechanism are illustrated and discussed in Figure 10. ii. As mentioned earlier, Te atom chain has a helical structure connected by strong covalent bonds, which can project as an equiaxial triangle shape on its cross-sectional plane [27]. When a compressive or tensile force is applied on the Te atom along the Te NWs' thickness direction (y-axis) in its cross-sectional plane, it will cause the equiaxial triangle to transform into an isosceles obtuse or acute triangle shape respectively. Both the obtuse and acute triangles can cause a dislocation of the positive Te ions and the electronic negative charge center, in result of downward or upward transferring of electrons to form a balancing piezoelectric potential [27]. Te NWs are formed by connecting groups of Te atom chains in hexagon structure bounded by weak van der Waals bonding force [27, 49, 50]. Theoretically speaking, when a force is only applying in x and y direction, the piezoelectrical polarization forms due to the asymmetry of the Te crystallographic structure, whereas the overall piezoelectrical

potential on the NWs could not exist when applying force in z direction due to the offset of localized piezoelectrical potential. Such concept and result have been reported [27, 51, 52]. The flexible PE bio-skin device is printed in lines that form a certain structure as a planer integrity, in which Te NWs are aligned along the lines during the printing process. A similar manner of generating piezoelectrical polarization through applying force to deform Te atom in x or y direction can be implemented by compressing or stretching the device in different directions, resulting in an upward or downward charge transfer in the circuit, respectively. In summary, the electricity generated by TE bio-skin is due to the external force applied that is able to cause the contact and separation between two dissimilar materials of the opposite polar, such as the negative PDMS and positive medical plastic tape in this research; For PE bio-skin, the electrical functionality is owed to the piezoelectric material itself, such as the Te NWs used in this research, by applying a deforming force on the structure of the TE NWs to cause the formation of piezoelectric potential to balance the external force.

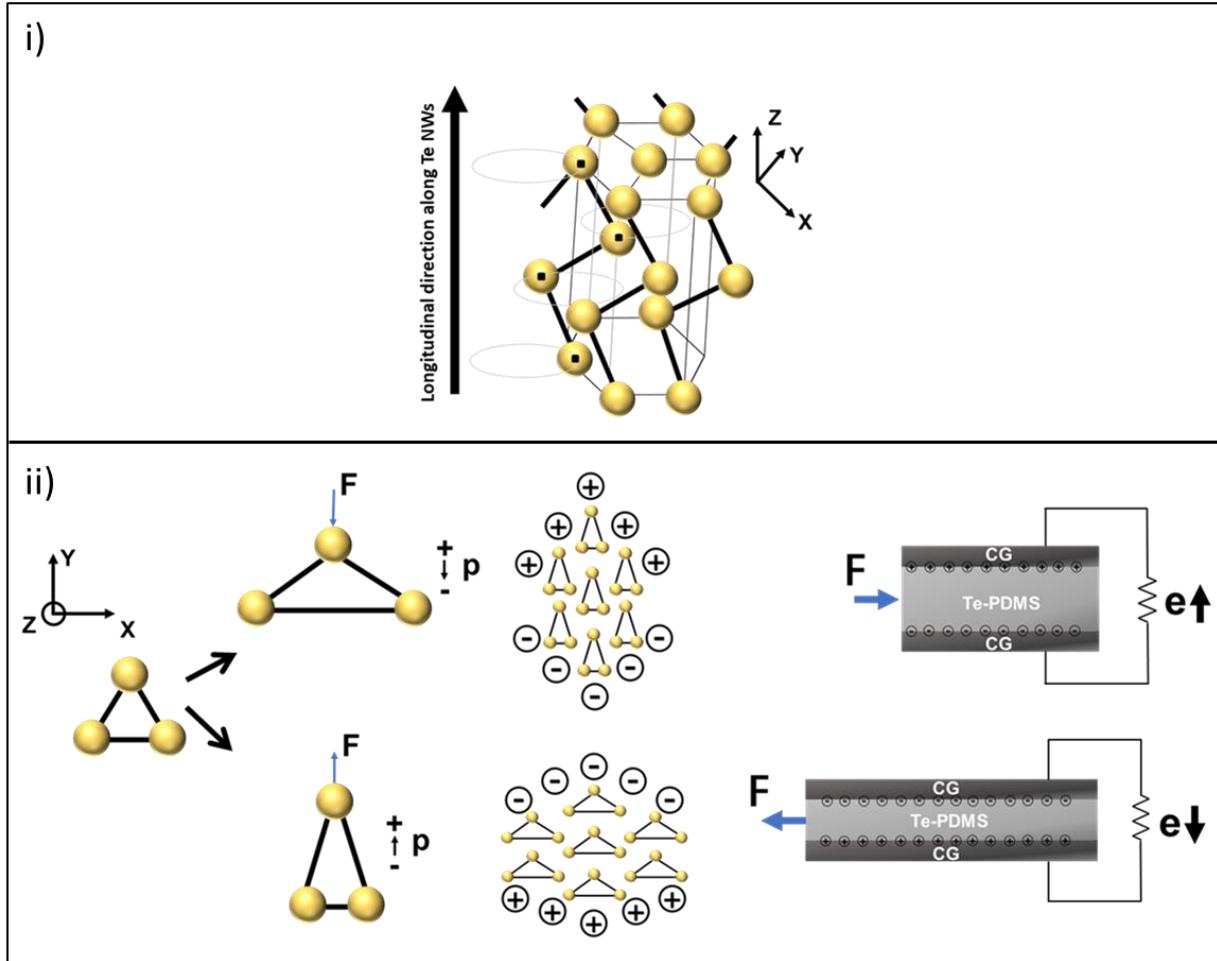


**Figure 10.** The operating mechanism of the PE Bio-skin

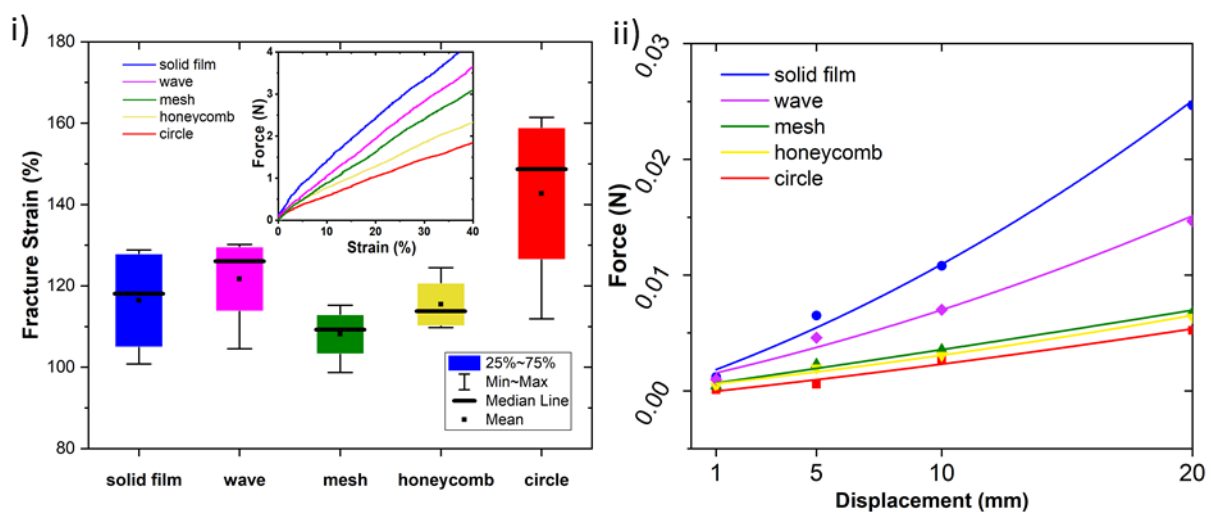
### 3.3 Results from TE Bio-skin Optimization Process

During the structure optimization process, except for the solid structure that can be achieved by most of the traditional fabrication techniques for electrical devices, the 4 base structures (Chapter 2.4) were designed based on the concept in which the base structure should be made air-permissible and more stretchable than the solid film. Figure 11 shows the Maximum strain, Force-Strain curve, and Force-Displacement curve from the experiments and FEA simulation results of the 5 structures.

The strain from the experiment can be represented by the calculation:  $\frac{\text{elongated length}}{\text{effective length}} = \frac{\text{elongated length}}{30.52\text{mm}}$ . The maximum strain and tensile force experiment results can be found in T1 from

Appendix A3. Averagely, the tensile test result (Figure 11.i) shows the circle structure yields to the largest maximum strain of 142.68%, and such structure also shows better elasticity, which is a

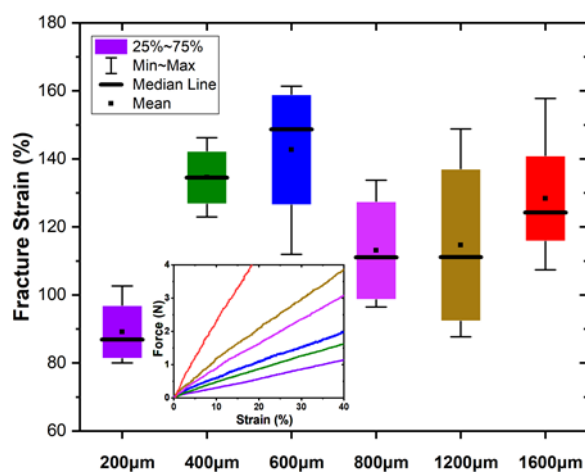
lower elastic modulus, than other structures based on the slope of Force-Strain curves. The result could be due to the diminished local stress applied on the corners in the circle structure during the elongation process. FEA simulation (Appendix A4) of the 5 structures with hyperelastic material is also demonstrated to prove the circle structure requires the least elastic modulus and force to reach a certain displacement as shown in Figure 11. ii. The circle structure design was selected to be the ideal model for the 3D printed TE bio-skin, as it can effectively reduce the elastic modulus when attached and stretched with human skin on uneven surface or movable joints, and its maximum strain can guarantee the applicability as stretchable smart sensor in most forms of human movements.



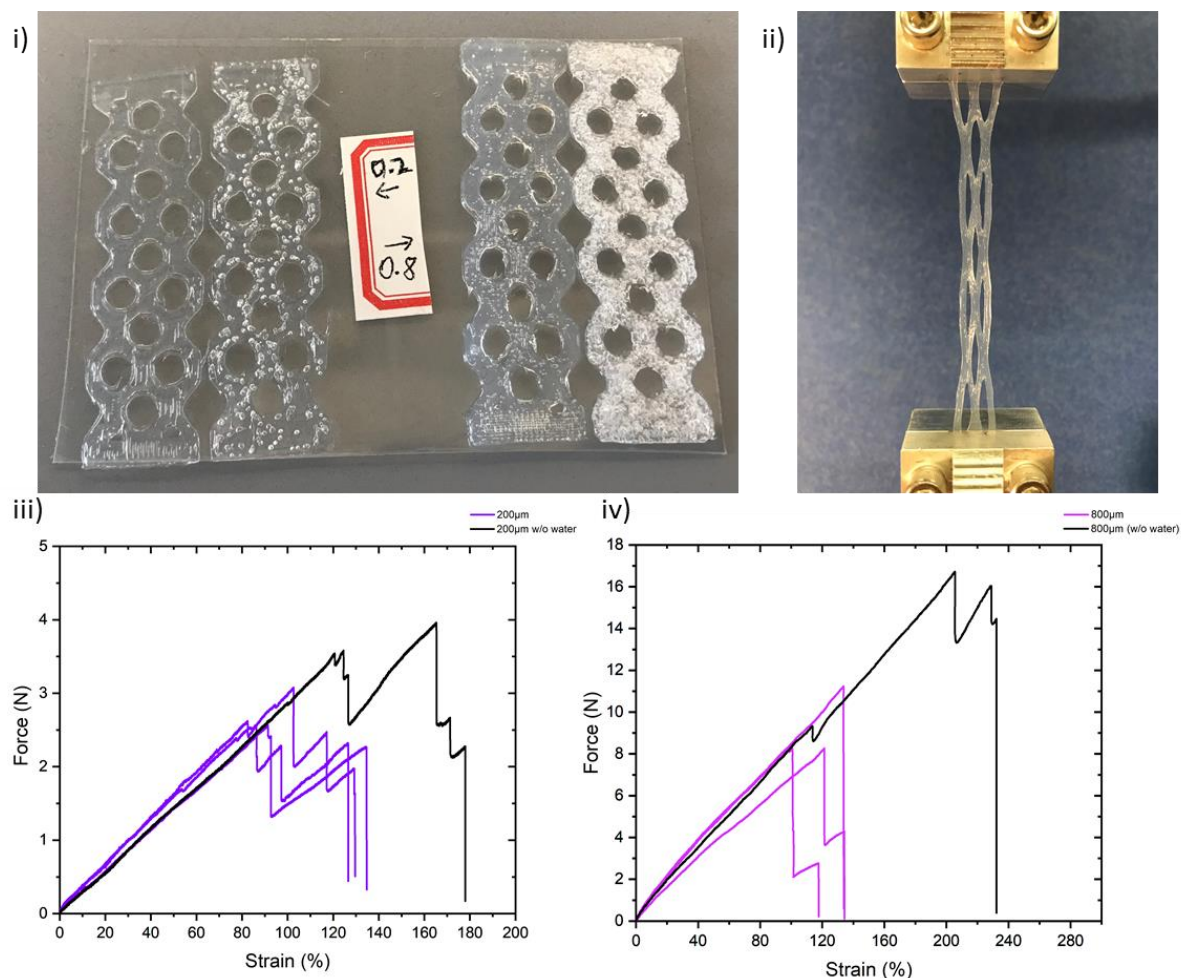
**Figure 11.** Tensile Comparison from Experiment and FEA Simulation with hyperelastic material (Right) of 5 structures

Figure 12 shows that the Force-Strain ratio increases with increasing thickness based on the data collected in T2 from Appendix A5, but the sample with  $600\mu\text{m}$  thickness yields to the largest maximum strain, which could be due to the defect of water mixed into PDMS for reducing the viscosity in printing. Ideally speaking, the maximum strain of PDMS is related to the yield strength, which is a material property that does not change with thickness, but during the experiment the air bubbles as a defect factor in the PDMS could potentially change the mechanical strength property that could be a failure point for the maximum strain of the structure at various thicknesses. From the experiment it has also been proven that if the material is printed too thin, the air bubble defects

caused in the printing and curing process could be a dominant factor for the change of strength of the material, which will prevent it from reaching a large strain. In order to decide the most suitable thickness of the PDMS used in the device by selecting the soft but also elastic structure, the most optimal thickness applied on the final device is suggested in the range of  $400\mu m \sim 800\mu m$  based on the result. It is noticed that the water can cause a non-uniform curing in PDMS due to the formation of air bubbles from evaporation, which will result as a non-transparent look of the samples in Chapter 2.4. Figure 13.i shows two PDMS samples printed with or without water. The left and right pair of samples were printed with a thickness of  $200\mu m$  and  $800\mu m$  respectively, and the left side in either pair was not mixed with water. After curing, few air bubbles exist inside the non-water samples. The air bubbles are not significantly affecting the young's modulus and the slope of Force-Strain curve of the samples, but the non-water samples can reach a larger maximum strain as shown in Figure 13.ii-iv. Since water can effectively reduce the viscosity of PDMS matrix for the ease of printing process, to compromise, the distilled water was reduced to 0.5g in the preparation of PDMS mixture.



**Figure 12.** Tensile Comparison from circle structure of 6 thicknesses



**Figure 13.** Samples Printed with/without Water in PDMS Mixture and Tensile Comparison

As a result, previous 3D printed TE bio-skin of mesh structure was optimized by selecting circle structure and printing 3 base layers of PDMS mixture with reduced water, embedding 1 layer of carbon grease and covered with small hemispheres pattern of same size from earlier design. The CAD model and printing of the optimized TE bio-skin is shown in Figure 14.i. Figure 14.ii shows the phase that optimized TE bio-skin was starting tensile test and its maximum strain. As shown in Figure 13.iii, compared to previous TE bio-skin, which averagely has a maximum strain of 47.33%, and a lateral Force-Displacement of 0.36N/mm, the optimized TE bio-skin shows greatly enhanced mechanical performance with a maximum strain of 151.67%, and a lateral Force-Displacement of 0.21N/mm (T3 from Appendix A6).

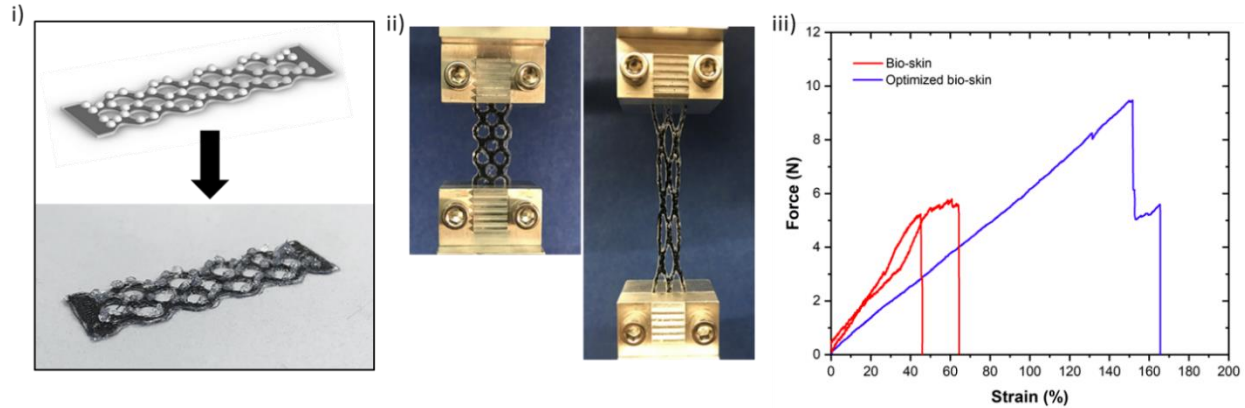


**Figure 14.** Optimized TE Bio-skin and Tensile Comparison with Unoptimized TE Bio-skin

### 3.4 Electrical Characterization of the Bio-skin

#### (A) Optimized TE Bio-skin

The electrical characterization of the optimized 3D printed TE bio-skin were investigated with linear motor by making oscillatory touch between the medical plastic tape and TE bio-skin. Figure 15.i-iii show the graphs of  $I_{SC}$ ,  $V_{OC}$ , and  $Q_{SC}$  respectively. After tested, the TE bio-skin can reach an average current of 14nA, potential difference of 6V, and transferred charge of 2nC, which showcase the ability of the optimized TE bio-skin for electricity harvesting through triboelectric effect, and potential for sensing purpose. Figure 15.iv shows the output power and current of TE bio-skin with external loads of different resistance. It can be seen that the current is resistance-dependent, but maximum power will reach at 36.36 nW at 600M $\Omega$ . Detailed current and voltage data can be found in T4 from Appendix A7.

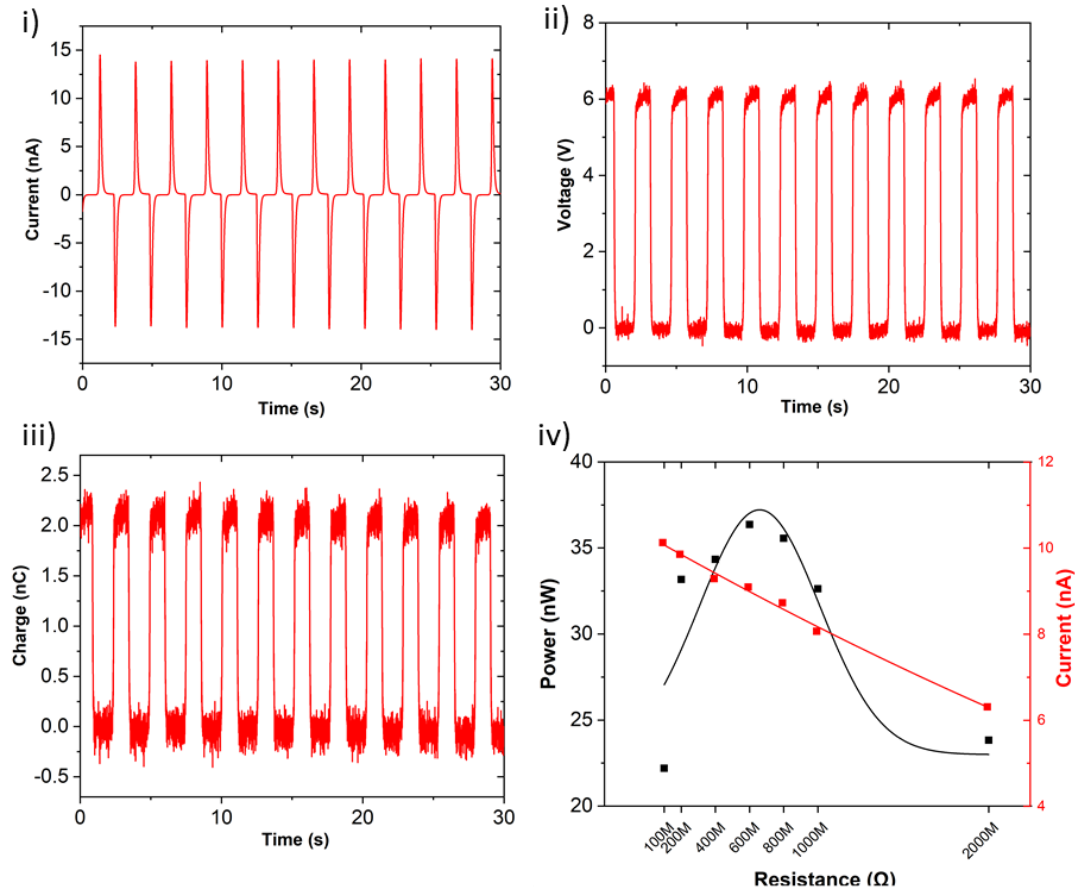


**Figure 15.**  $I_{sc}$ ,  $V_{oc}$ ,  $Q_{sc}$  of the Unstretched TE Bio-skin and its Output Power with Varying Resistance of External Loads

In addition, we have also proved the durability of TE bio-skin after it has been tested for 2000 cycles and its  $V_{oc}$  still remains constant as shown in Figure 13.i, such robust mechanical durability and electrical integrity guarantees TE bio-skin's long-term use in the contact mode. Another investigation on the electrical signal from the device in stretching mode and contact mode was tested, Current and voltage were measured as shown in Figure 13.ii for stretching mode and contact mode respectively. The results indicate that the electrical signal increases with enlarging pressure and elongation, demonstrating the utilizable electrical property on the human skin. For instance, when the TE bio-skin was attached to a movable joint, the TE bio-skin should be able to response with the different degree of stretching accordingly. The contact mode can be used to detect subtle movements such as heart pulse rate, voice, breath etc. with or without the TE bio-skin stretched.

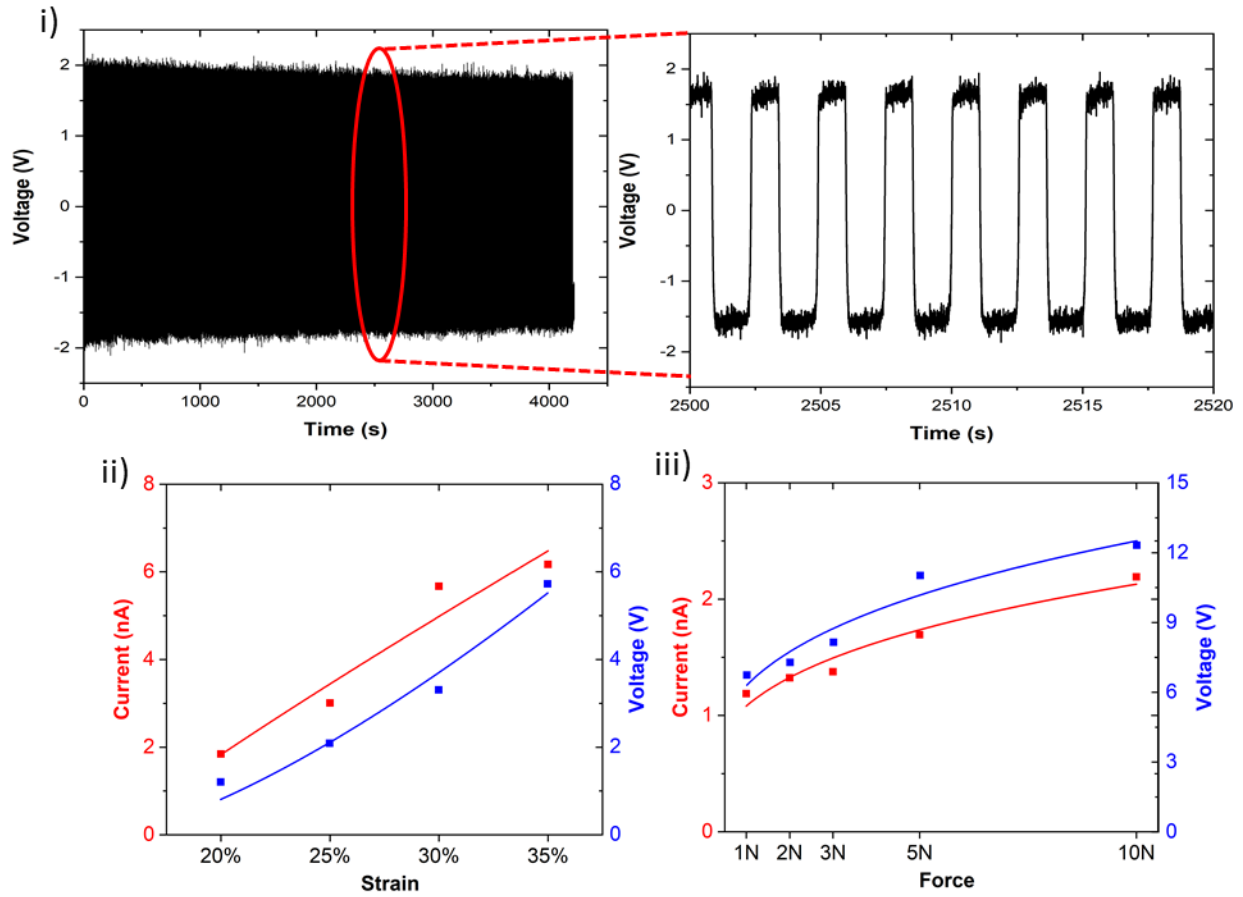


**Figure 16.** Electrical Durability Test and Dual Modes Test of the TE Bio-skin

## (B) PE Bio-skin(s)

To characterize the electrical outputs, both ends of the Te-PENG were clamped tight with two clamps, one of which was affixed on a L-bracket, and the second was fixed on the linear motor (LinMot) to periodically stretch and release the device horizontally with an oscillatory frequency set to be 0.5 Hz. The electrometer was used to measure the voltage  $V_{oc}$  from the device. A low-noise preamplifier was used to measure the current  $I_{sc}$ . Te-PDMS mixture has a similar silver-gray color as the synthesized Te-NWs products do, but pure PDMS matrix mixed with curing agent only is crystal clear. Figure 17.iv and v show the printed devices of Peano structure with or without Te NWs mixed into PDMS (middle layers) respectively. PE bio-skin devices in the 3 structures (Peano, Hilbert, and Sierpinski) were printed for electrical comparison. The devices were repeatedly stretched 20% with a frequency of 0.5Hz. Figure 17.i-iii show the measured electrical output  $I_{sc}$  (left) and  $V_{oc}$  (right) of devices in Peano, Hilbert, and Sierpinski structures respectively, among which the best electrical performance of the device in Peano structure has a maximum current  $6.15nA$  and a maximum voltage  $2.85V$ . The  $I_{sc}$  and  $V_{oc}$  measured from the device in Peano structure, with the absence of Te NWs, were also measured as shown in Figure 17.vi. Exploiting the 3D printed PE bio-skin in Peano structure as our final device design, the output power and current from the device were measured with the external loads of resistance in the circuit. It shows the current is resistance-dependent, and the maximum power can reach  $11.32nW$  at  $400M\Omega$  (Figure 18.i). Additionally, the electrical signal from the device is also proven to be strain-related by stretching it from 20% to 50% as shown in Figure 18. ii. The durability of the PENG in Peano structure was tested for 1500 cycles by stretching (30% strain) and releasing on the linear motor, and the result shows a constant  $I_{sc}$  output (Figure 18.iii).

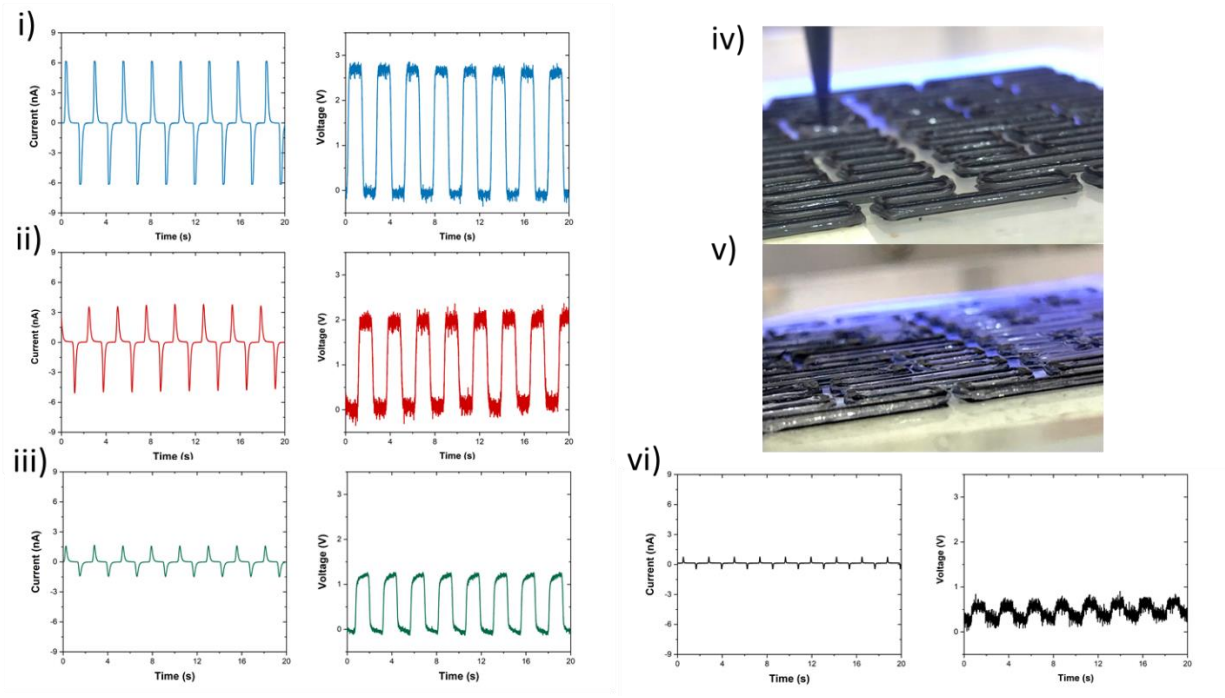


Figure 17.  $I_{SC}$ ,  $V_{OC}$  of the PE Bio-skin(s) and Without Te NWs

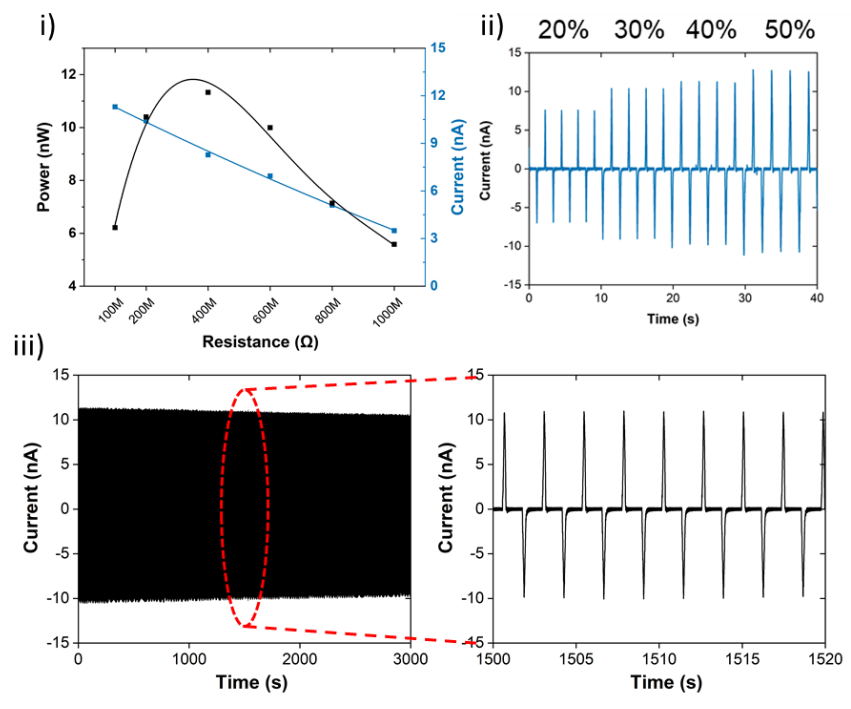


Figure 18. Electrical Power, Strain-responsive Signals, and Durability Test of the Peano PE Bio-skin

## CHAPTER 4. DEMONSTRATION

We investigated the performance of the TE bio-skin and PE bio-skin for detecting human's heart pulse rate, sound waves of speech, and bending movements through triboelectric and piezoelectric effects respectively. Chapter 4.1 and 4.2 are to demonstrate the application of the optimized TE bio-skin and Peano PE bio-skin in monitoring the health status of the human body through detecting central pulse and peripheral pulse from neck and wrist respectively, and subtle vibrations of human voice cord for distinguishing speech patterns. Chapter 4.3 is for detecting different degrees of large movements from the joint of human's elbow with TE bio-skin only.

### 4.1 Heart Pulse Rate Measurement and Health Monitoring

#### (A) Optimized TE Bio-skin

The heart pulse measurement was under contact mode of the TE bio-skin. Similar to the setup and working principle and method in electrical characterization, a piece of medical plastic tape with the same length of the optimized 3D printed TE bio-skin was cut off and stuck onto another piece of tape with longer length, make sure its non-stick side was in contact with the small hemispheres patterned on top of TE bio-skin. The device with the tape in contact was then taped tight onto the neck or wrist area of human body. Copper wire was inserted into the carbon grease for output signal measurement. Pre-amplifier was used to measure current signal in real-time. The tape and TE bio-skin were attached tight to the detecting area on wrist or neck with another medical plastic tape. Figure 19.i and ii. show the participant's heart pulse rate was successfully detected by the TE bio-skin on the neck and wrist respectively. They also show real-time measurement of heart pulse rate obtained from neck (Appendix A8) and wrist respectively in a 15-second period. It is noticed that, through both neck and wrist, human's heart pulse rate can be successfully detected on central pulse and peripheral pulse, which clearly shows two distinguishable factors that are used to evaluate human's physical condition: systolic peak ( $P1$ ) and point of inflection ( $P2$ ) [53,54]. Such quantifiable parameters can be used to calculate radial augmentation index ( $AI_r$ ) for assessment of human's cardiovascular system, which most commercial sensors are not capable to do.

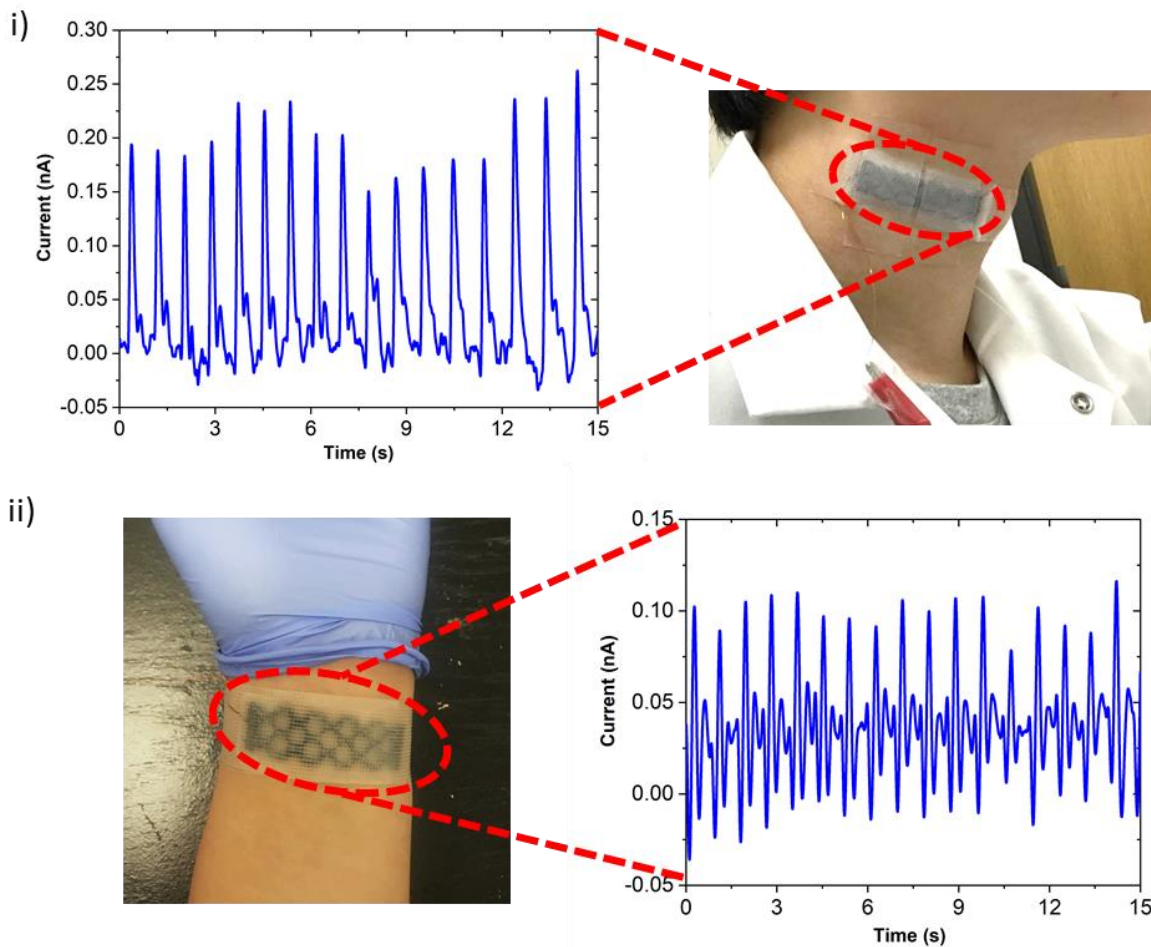


**Figure 19.** Heart Pulse Rate Measurement on Neck and Wrist with TE Bio-skin

Figure 15.i and ii show one single cycle of heart pulse rate signal measurement from neck and wrist respectively. For central pulse measurement from the neck,  $P1$  and  $P2$  are indicated at the peaks Upstroke Time ( $T_{up}$ ) is indicated as the duration to reach to  $P1$ ; Transit Time ( $\Delta T$ ) is defined as the time duration between  $P1$  and  $P2$ , which is proportional to the height ( $h$ ) of human beings.  $AI_r$  can be found by calculating the ratio of  $\frac{P2}{P1}$  to reflect the health status of human. Based on the chart of Relationship of the augmentation index to age [55], a healthy male person under his forties should have  $AI_r$  in a range between  $23.4 \pm 8.4\%$ . The participant has an average central pulse  $AI_r = \frac{\sum_{i=1}^{14} \frac{P_{i2}}{P_{i1}} \times 100\%}{14} = \frac{3.166}{14} = 22.62\%$  that meets the requirements of healthy status. Additionally, average  $\Delta T$  is from the time interval difference between  $P2$  and  $P1$  in each heart beat rate cycle

can also be calculated:  $\Delta T = \frac{4.134}{13} = 0.260s = 260ms$ . Peripheral pulse has an average  $\Delta T = 326ms$ , and the index of large artery stiffness  $SI$  can be derived from the ratio of participants height  $h$  and  $\Delta T$  from peripheral pressure pulse,  $SI = \frac{h}{\Delta T} = \frac{1.78}{0.326} = 5.46m/s$ , which is similar to the stiffness result measured from carotid-femoral pulse wave velocity (PWV). The result obtained from the participant is corresponding to the profile and statistics [56] to show his healthy status was maintained within the range suggested below his 29 years age. Lastly, the upstroke time  $T_{up}$  is an important indicator of aortic stenosis. The participant has an average central pulse  $T_{up} = \frac{3.636}{14} = 0.126s = 126ms$ , and the result is closed to the statistics collected from healthy volunteers [57]. Both ways of measuring pulse show a similar heart beat rate  $73 \pm 1$  beats/min (bpm), within the normal distribution range of  $69.7 \pm 10.8$  bpm of a healthy person under his 40 years of age.

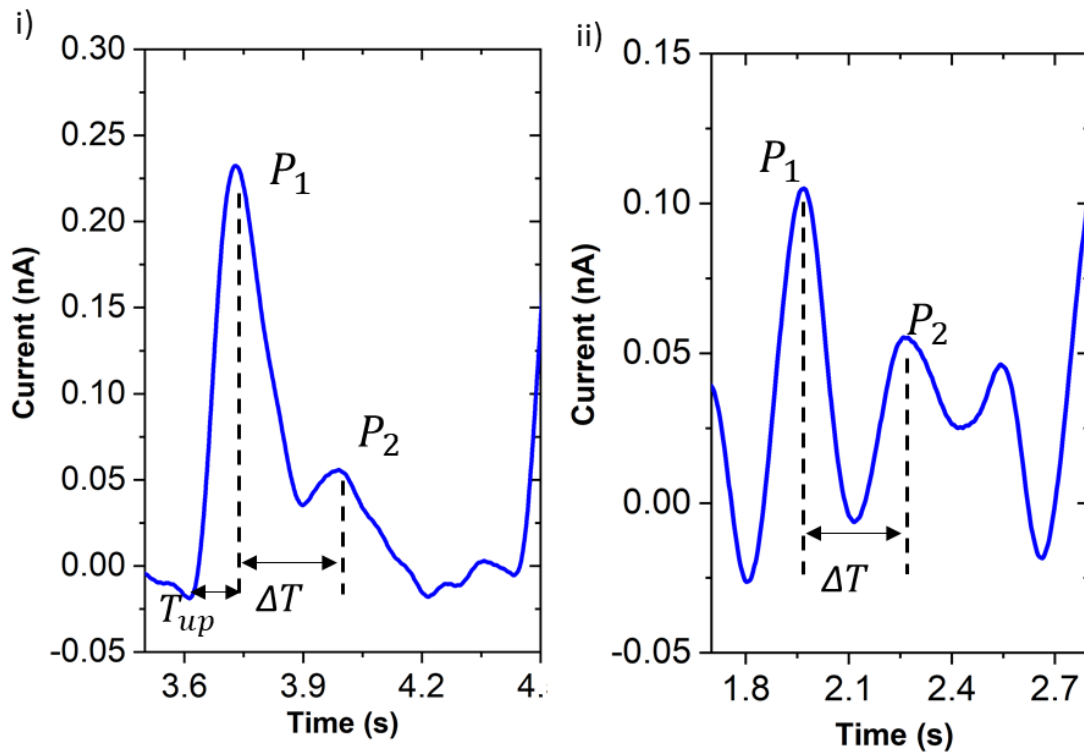


**Figure 20.** One Period Cycle of Heart Pulse rate Measured from Neck and Wrist with TE Bio-skin

(B) Peano PE Bio-skin

Through mechanical properties investigation, Peano PE bio-skin was selected as the best candidate for the demonstration utilizing piezoelectric polarization. To collect the heart pulse detection signals, similarly to the TE bio-skin, the Te-PENGs were taped against the wrist and neck respectively with a double side tape. Figure 21.i and ii show the human peripheral heart pulse and central heart pulse were detected by the device attached on wrist and neck (A9) respectively. A 10-second period of heart pulse was collected from the participant from his wrist or neck, where  $P1$  and  $P2$  are obviously detected on the heart pulse profiles as shown in Figure 22.i and 15b. ii. Through calculation from collected data by Peano TE bio-skin., the participant has an average central pulse  $AI_r = \frac{\sum_{i=1}^{i=9} \frac{P_i^2}{P_i^1} \times 100\%}{9} = \frac{2.6841}{9} = 29.82\%$  and an average  $T_{up} = 119.25ms$ , which are within the normal range from previous references. For the peripheral heart pulse electrical signals measured from wrist,  $\Delta T = \frac{2.74}{9} = 0.304s = 304ms$ , and  $SI = \frac{h}{\Delta T} = \frac{1.78}{0.304} = 5.85m/s$ , and the result is also closed to the suggested statistics reported for a healthy male below his age of 29. Additionally, the device can easily detect the heart beat rates measured from wrist and neck were 61.3 and 72 beats/min (bpm), satisfying the normal range of  $69.7 \pm 10.8$  bpm for human heart rate below his age of 40.

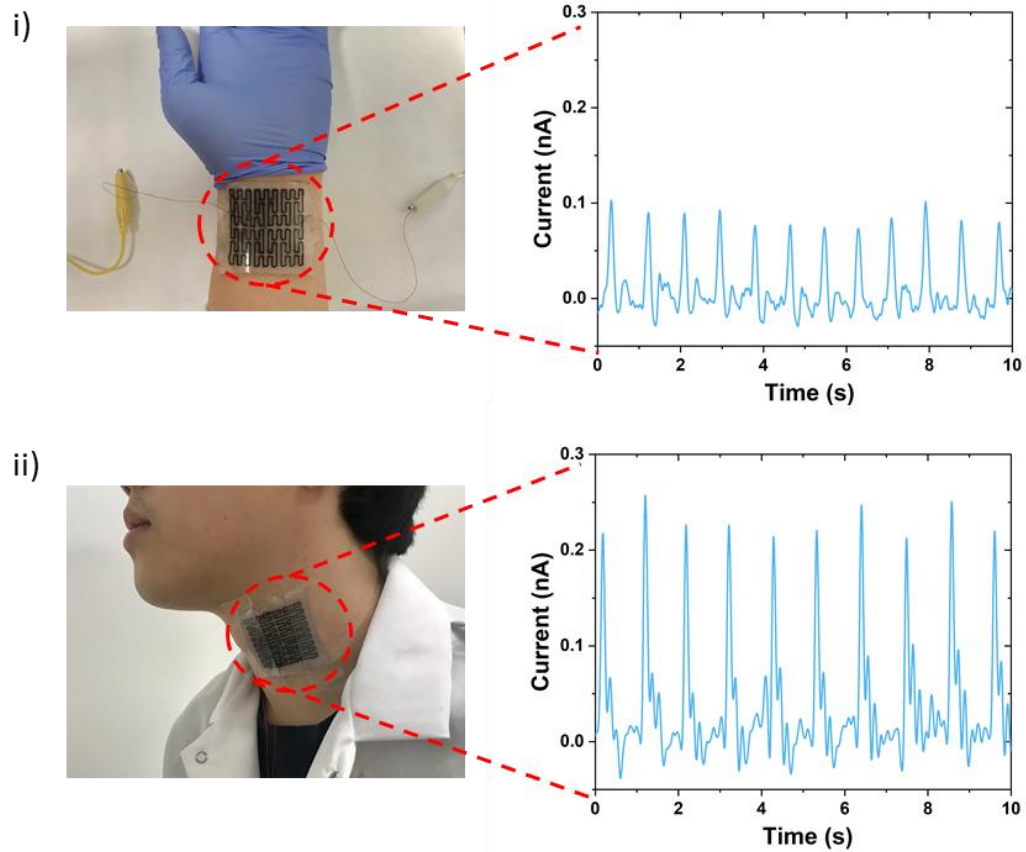


**Figure 21.** Heart Pulse Rate Measurement on Neck and Wrist with PE Bio-skin

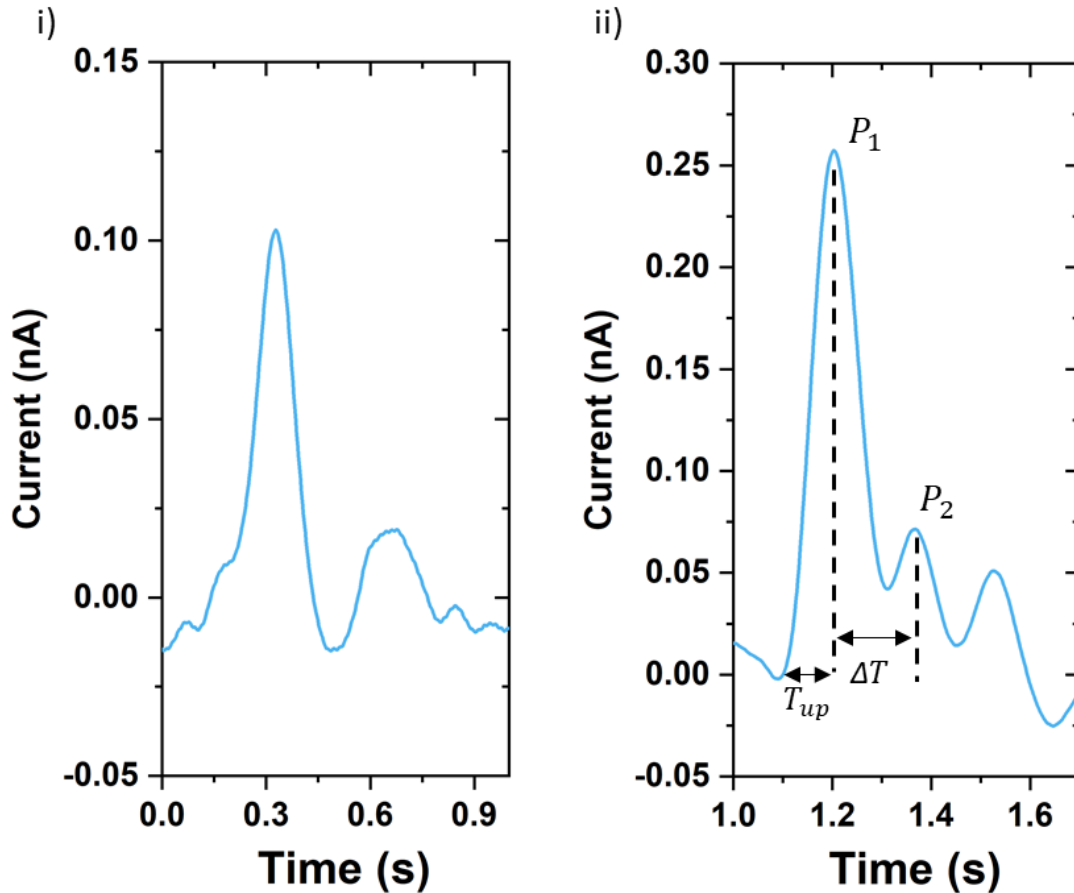


**Figure 22.** One Period Cycle of Heart Pulse rate Measured from Neck and Wrist with PE Bio-skin

#### 4.2 Detection on Human Acoustic Waves

Besides the clinical significance proven by both bio-skin devices, we also demonstrated the capability of the TE bio-skin and PE bio-skin for monitoring sound waves by the subtle vibration from the human voice cord, which can be further integrated as a voice sensor to collect speech patterns for recognition.

##### (A) Optimized TE Bio-skin

In this demonstration, similar to the previous heart pulse detection experiment, the optimized TE bio-skin was taped around the human voice cord area on the neck, covered by the non-sticky side of a piece of medical plastic tape attached on another piece. The voltage signal was collected with a frequency filter between 3Hz-1000Hz. 3 words ‘Purdue’, ‘Boiler’, ‘Up’ were repeatedly

pronounced by the participant for 5-6 times as shown in Figure 23.i. The voltage electrical signals of the 3 words were further analyzed with Fast Fourier Transform (FFT) for comparison:

$$X_k = \sum_{n=0}^{N-1} x_n e^{-\frac{i2\pi kn}{N}} = \sum_{n=0}^{N-1} x_n \omega^{-kn}, k = 0, 1, 2, \dots, N - 1$$

Where  $\omega = e^{-\frac{i2\pi kn}{N}}$ , which is the first complex N-th root of 1. After calculating, the FFT wavefunctions of the 3 words and background noise from the collect electrical signals were plotted as shown in Figure 23. ii. It is noticed that the filtered signals still have electrical harmonics occurred at integer multiples (1, 2, 3...) of the fundamental frequency 60Hz as a background noise. Besides that, the FFT result of the 3 words clearly show the distinguished waveforms with peak(s) at different frequencies and voltage magnitudes.

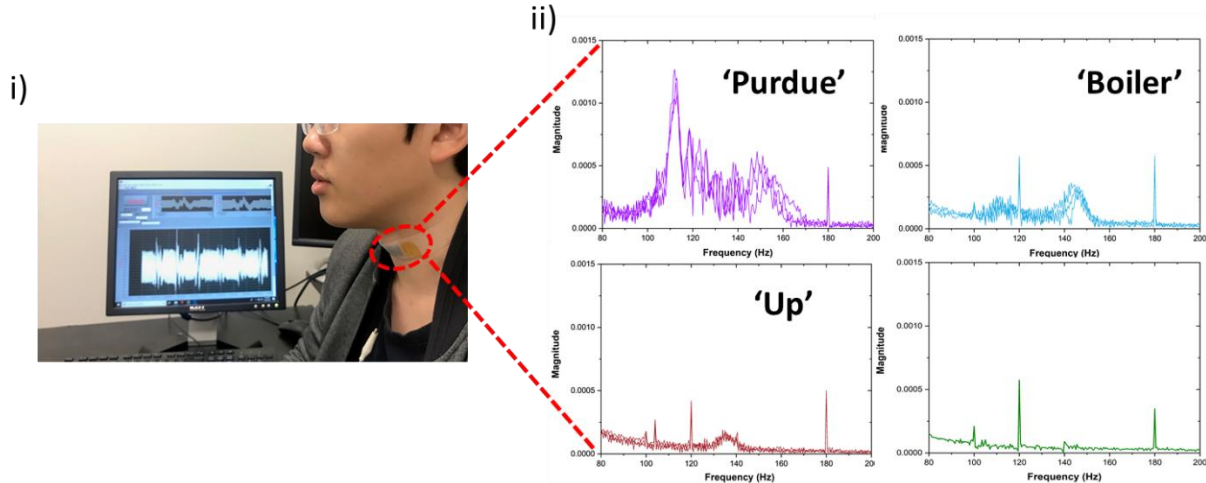


**Figure 23.** Speech Recognition with FFT analysis of the 3 words ('Purdue', 'Boiler', 'up')

The average FFT result shows 'Purdue' can reach 2 peaks at 113 Hz and 151 Hz, with electrical magnitudes of 11 E-4 and 4 E-4 respectively; 'Boiler' also reaches 2 peaks at 112 Hz and 145 Hz, with the magnitudes of 2 E-4 and 3 E-4 respectively; 'Up' reaches 1 peaks at 135 Hz with a magnitude of 1.5 E-4 only (Figure 24.i). The difference of peaks and magnitudes of different words from the signal data collected by the TE bio-skin shows promising utilization for the distinguish of speech wave functions. Additionally, to visualized the difference of the speech patterns, the electrical signals were further processed into voice spectrograms for speech identification, where the pattern for each word is unique and repeatable for recognition purpose (A10). Figure 24.ii shows a typical result of the spectrograms demonstrating the recognition of

the 3 words based on the electrical signal collected by the TE bio-skin. Such results can be promising for future application, such as integrated into a comfortable, flexible and wearable speech sensor for human-machine interaction system.

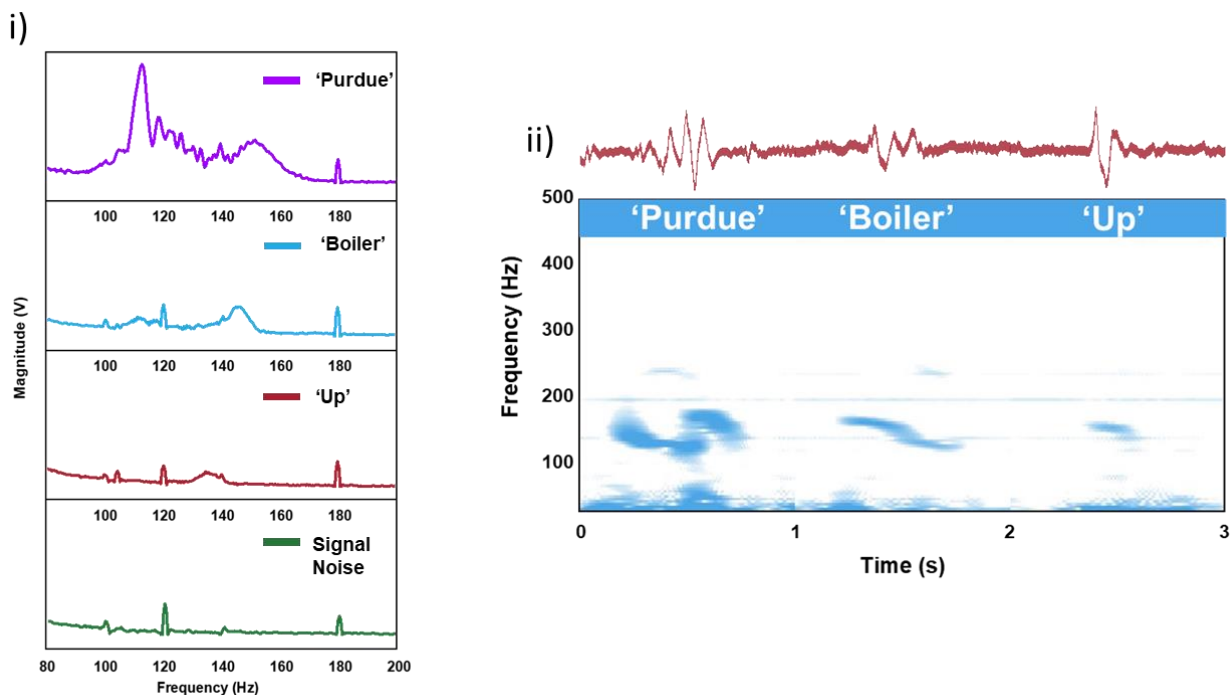


**Figure 24.** Average Wavefunction and Voice Spectrogram

#### (B) Peano PE Bio-skin

Similar to the TE bio-skin demonstration, the Peano PE-PENG was taped around the human voice cord area. Voltage signal was collected with a frequency filter between 3Hz-1000Hz. 3 words 'Purdue', 'Giant', 'Leaps' were repeatedly pronounced for 5-6 times. Figure 25.i shows the 3D printed Te-PENG was attached to the participant's voice cord area on the neck. The voltage electrical signals of the 3 words were further analyzed with Fast Fourier Transform (FFT) to calculate the average FFT results of the 3 words (Figure 25.ii), which also clearly show the distinguished waveform with peak(s) at different frequency and different voltage magnitudes. Figure 25.iii shows a typical result of the spectrograms of the 3 words which were plotted to easily identify the speech patterns, detailed spectrograms of the other samples can be found in A11.

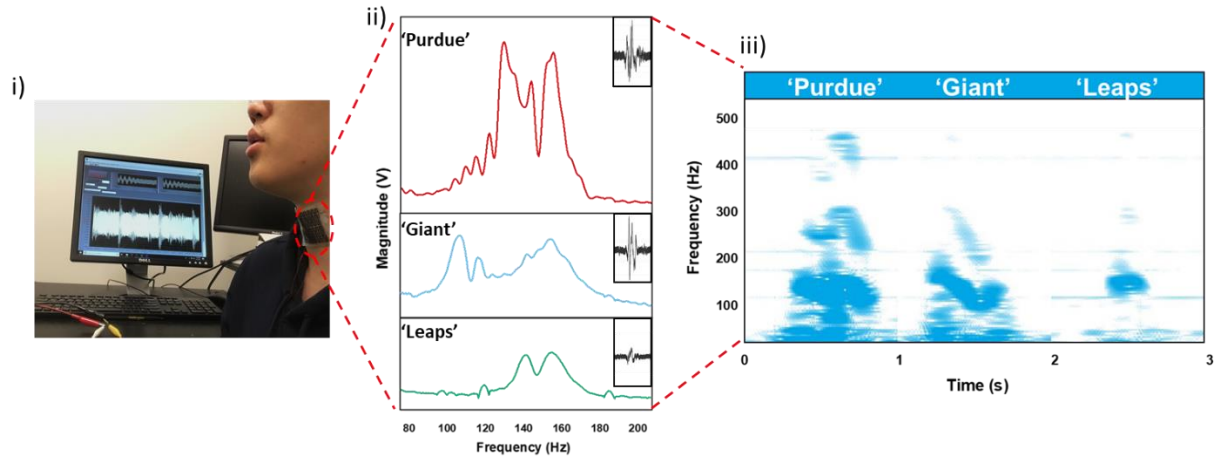


**Figure 25.** Average Wavefunction with FFT analysis of the 3 words ('Purdue', 'Giant', 'Leaps') and Voice Spectrogram

#### 4.3 Detection on Large Degree of Body Movements

Figure 26 demonstrates the performance of the optimized TE bio-skin for detecting large movements from human body under its stretching and contact mode in a bending motion. The TE bio-skin was taped tight under the elbow joints of straight arm. An elastic medical band attached with the medical plastic tape was covering to touch the hemisphere surface of the TE bio-skin as shown in Figure 26. ii. The arm was recurrently bent to  $150^\circ$ ,  $90^\circ$  and  $30^\circ$  respectively to measure the electrical signals in Figure 26.i. Figure 26. iii shows distinguished electrical outputs of the 3 angles according to different degrees of bending, which proves the stretchability and functionality of the device. In summary, the dual mode optimized 3D printed TE bio-skin was demonstrated to be able to detect heart pulse rates through obvious systolic peak and evaluating human's health status, detecting speech patterns from human voice, and detect large movements with its fine flexibility.

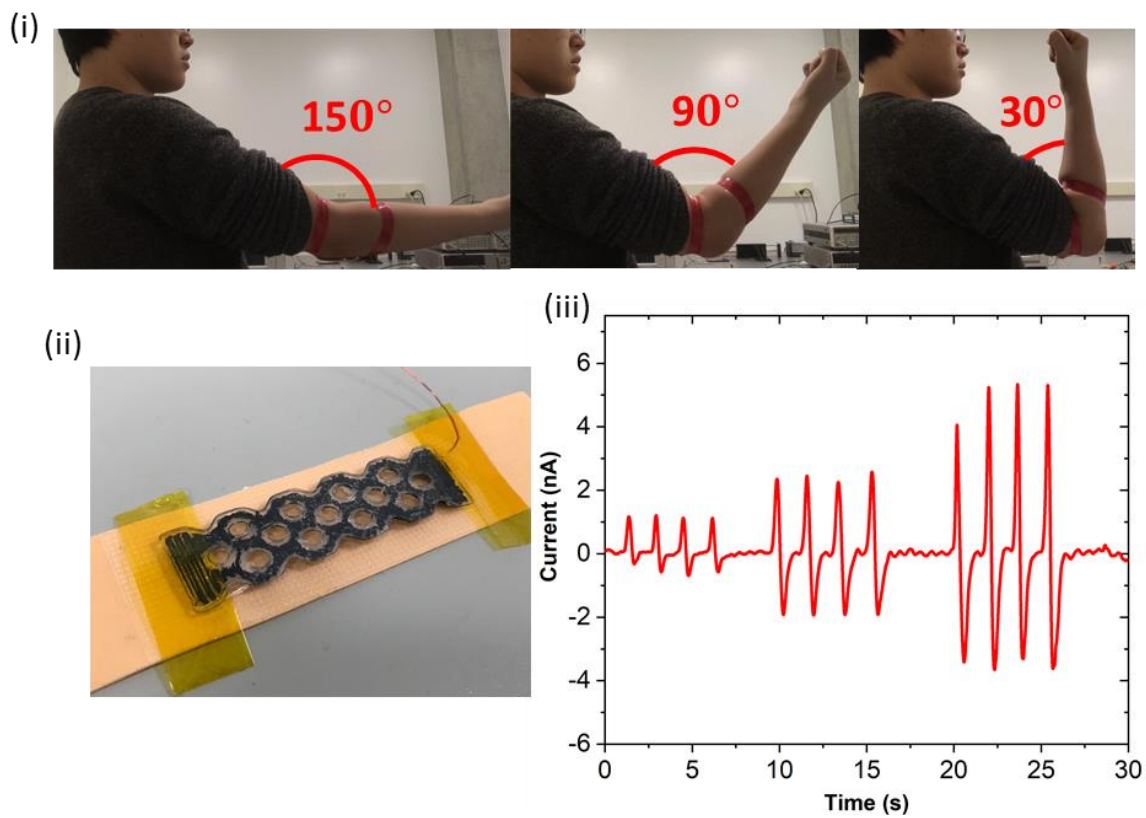


**Figure 26.** Detection of Different Bending angles from the Participant's Elbow

## CHAPTER 5. CONCLUSIONS AND RECOMMENDATIONS

### 5.1 Conclusions

In summary, we have presented a novel flexible electrical sensor fabrication method with inkjet 3D printing technique that utilizes piezoelectric polarization and triboelectrification principle to harvest small mechanical energy and detect subtle movements from human bodies. Both TE bio-skin and PE bio-skin devices are designed in a rational and customized manner, and printed with dual extruders with multiple materials without further human intervention for assembly. The low-cost materials PDMS matrix and fluidic carbon grease used for TE bio-skin in this study are proved to be easily printable, bio-compatible, mechanical flexible and robust. The design and thickness selection of the device are optimized through tensile study. The printed device also possesses excellent triboelectric property that the device can reach a satisfying electric output for sensing purpose. For the PE bio-skin, Te-PDMS was used as the printing piezoelectric material by mixing synthesized Te NWs with PDMS matrix, in which the piezoelectric Te NWs were believed to be able to align perfectly along the printing path for an enhanced electrical output. PE bio-skin devices in different fractal structures are electrically compared. Both optimized TE bio-skin and PE bio-skin are proved to be electrically stable as well.

Such devices are demonstrated to effectively detect human's health status by monitoring the heart pulse rate on neck and wrist in real-time, and be capable of capturing human sound waves for speech recognition. The TE bio-skin is also demonstrated to utilize its proven stretchability to detect large movements from the human body. Both the bio-skin devices are safe and comfortable in wearing for human skin, and can be promising as a smart sensor for other potential applications, such as hand gesture recognition used in human machine interaction system. Since it has been tested that the word patterns from the voice spectrogram are repeatable for the only participant during the speech recognition process, another possible application using the bio-skin devices might be voice biometric authentication based on the voice recognition, as the voice frequencies are different from people to people, and the word patterns for a person could be much likely unique from others as well.

## 5.2 Study Gap and Recommendations

In this research of study, for the TE bio-skin device, due to the equipment limitation of the printing with dual extruders, the author has only achieved in the fabrication of the single electrode, one dielectric layer of the wearable electrical device with 3D printing technique. The subsequent assembly of the positive material, medical plastic tape, is still externally required for the operating of electrical function from the TE bio-skin. In the future of study, the author may search for printable and bio-compatible possible materials to fabricate a stretchable electrical device in integrity. Secondly, the device can continue to be developed on energy harvesting as power source by improving its electrical property through changing the density, size, or shape of the hemisphere pattern designed on top, and test on other promising application such as hand gesture recognition based on the current results. For the PE bio-skin device, the structure of some of the fractal patterns were designed to be anisotropic, as a result of unsystematic comparison in the electrical measurement with unidirectional stretching. In the future of study, the printing path design of PE bio-skin devices could be in symmetric orientation and control thickness of Ecoflex for mechanical improvements. Another gap can be found in the demonstration of heart pulse rate measurement from the neck, since there might be other factors such as breath that can affect the signal results of heart pulse waves. Suggested body part for measuring the central pulse could also be tested on the human chest. The 3 chosen medical criteria ( $AI_r$ ,  $T_{up}$ ,  $SI$ ) might not be sufficient for the purpose of human health assessment, and thus the bio-skin devices are more suitable for the goal of checking heart-related diseases, or assessing any regular abnormalities in the heart beats that could reflect a potential heart attack. In the future of work, the author is also suggested to include the data/profiles measured from a commercial heart rate detector for comparison with the signal results collected from the bio-skin devices. Though the bio-skin devices are proved to be bio-compatible and safe for human skin, and the smart structure design can increase the comfort level for human bodies due to the reduced elastic modulus of the devices, it is also recommended that the author should conduct surveys or reviews from the general public to better assess the acceptance level in which the bio-skin devices are applied on human skin, and in which extent the comfort level is satisfied in wearing the devices.

## APPENDIX

### A1 Printing process video

[Link1](#)

### A2 Triboelectric series chart

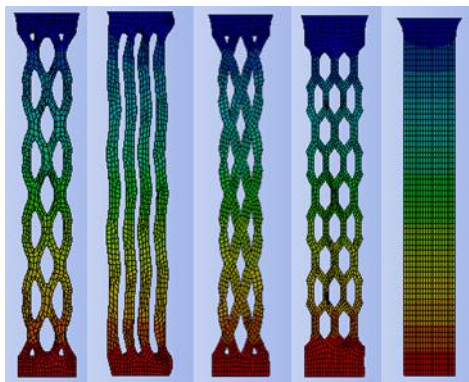
	Polyformaldehyde 1.3-1.4	(continued)
	Etylcellulose	Polyester (Dacron)
	Polyamide 11	Polyisobutylene
	Polyamide 6-6	Polyuretane flexible sponge
	Melanime formol	Polyethylene Terephthalate
	Wool, knitted	Polyvinyl butyral
	Silk, woven	Polychlorobutadiene
	Aluminum	Natural rubber
	paper	Polyacrilonitrile
	Cotton, woven	Acrylonitrile-vinyl chloride
	Steel	Polybisphenol carbonate
	Wood	Polychloroether
	Hard rubber	Polyvinylidene chloride (Saran)
	Nickel, copper	Polystyrene
	Sulfur	Polyethylene
	Brass, silver	Polypropylene
	Acetate, Rayon	Polyimide (Kapton)
	Polymethyl methacrylate (Lucite)	Polyvinyl Chloride (PVC)
	Polyvinyl alcohol	Polydimethylsiloxane (PDMS)
	(continued)	Polytetrafluoroethylene (Teflon)

*United States. Dept. of Energy. (2017). Triboelectric nanogenerator. Washington, D.C.*

### A3: Sample 1-4 for each structure (T1)

	<b>Solid film</b>	<b>Honeycomb</b>	<b>Circle</b>	<b>Mesh</b>	<b>Wave</b>
<b>Maximum strain (%)</b>	128.8521	124.4436	156.5895	110.8149	122.878
	109.0287	110.4406	140.8193	98.70391	129.2172
	100.7975	109.778	161.4012	107.6647	130.1865
	127.1426	117.116	111.9293	115.2326	104.5237
<b>Force (N)</b>	11.1966	6.04368	7.16659	7.87512	11.57
	10.31288	7.73116	6.2328	7.01502	10.80865
	8.01975	6.05476	5.96371	7.18048	10.41994

	11.40798	5.77663	5.33929	7.91544	8.42719
--	----------	---------	---------	---------	---------

**A4: simulation****A5: Sample 1-4 for thickness (T2)**

	200 $\mu\text{m}$	400 $\mu\text{m}$	600 $\mu\text{m}$	800 $\mu\text{m}$	1200 $\mu\text{m}$	1600 $\mu\text{m}$
<b>Maximum strain (%)</b>	102.651	138.5333	156.5895	121.3321	125.4806	124.2998
	91.2897	130.485	140.8193	100.7594	96.7441	107.3666
	82.4155	122.926	161.4012	96.418	87.678	124.1553
	80.0429	146.1977	111.9293	133.74	148.839	157.76
<b>Force (N)</b>	3.079219	7.28313	7.16659	8.274865	12.12506	16.73865
	2.573885	6.908554	6.2328	8.25565	12.56338	17.48325
	2.624038	4.913736	5.96371	7.520038	10.47718	16.73865
	1.950538	6.227509	5.33929	11.24415	16.73447	21.55429

**A6: Tensile test results of the TE bio-skin before and after optimization (T3)**

	Maximum strain (%)	Force (N)
<b>Optimized TE bio-skin</b>	151.67	9.47775
<b>Unoptimized TE bio-skin</b>	47.33	5.23916

**A7: Current and Voltage with variant resistance of external loads (T4)**

Resistance ( $\Omega$ )	Current ( $nA$ )	Voltage ( $V$ )
<b>100M</b>	10.13	1.532
<b>200M</b>	9.857	2.191
<b>400M</b>	9.289	3.365

<b>600M</b>	9.094	3.696
<b>800M</b>	8.728	3.998
<b>1000M</b>	8.067	4.074
<b>2000M</b>	6.313	4.044

**A8: Demonstration video of heart rate measurement on neck by optimized TE bio-skin.**

[Link 2](#)

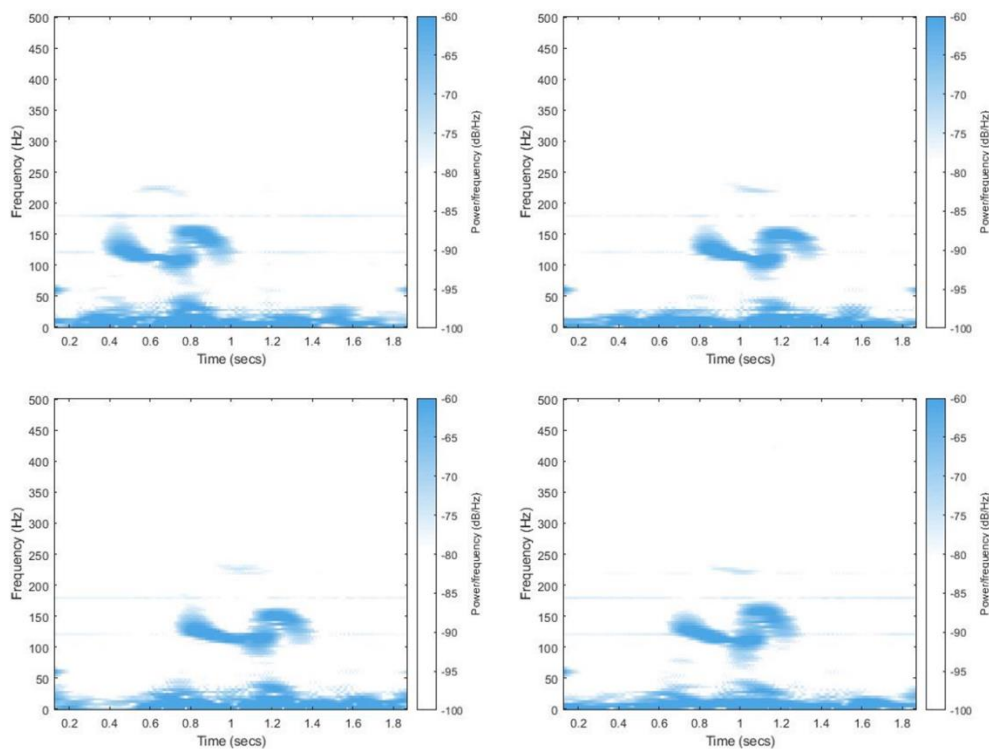
**A9: Demonstration video of heart rate measurement on neck and wrist by Peano PE bio-skin**

[Link 3](#)

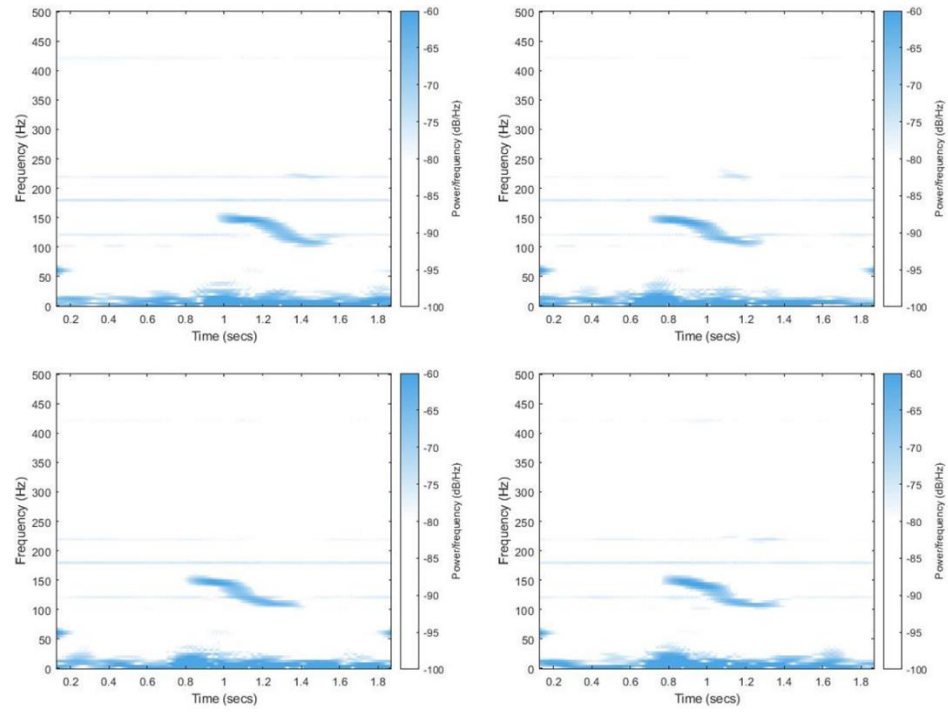
[Link 4](#)

**A10: Voice spectrograms for speech recognition from TE bio-skin**

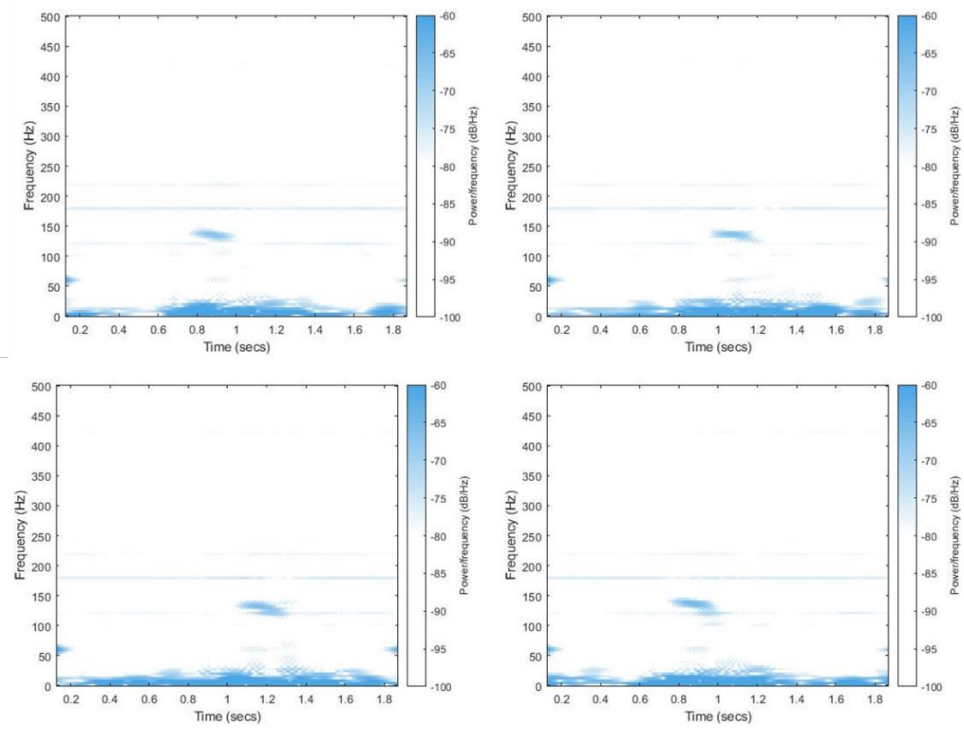
‘Purdue’:



‘Boiler’:

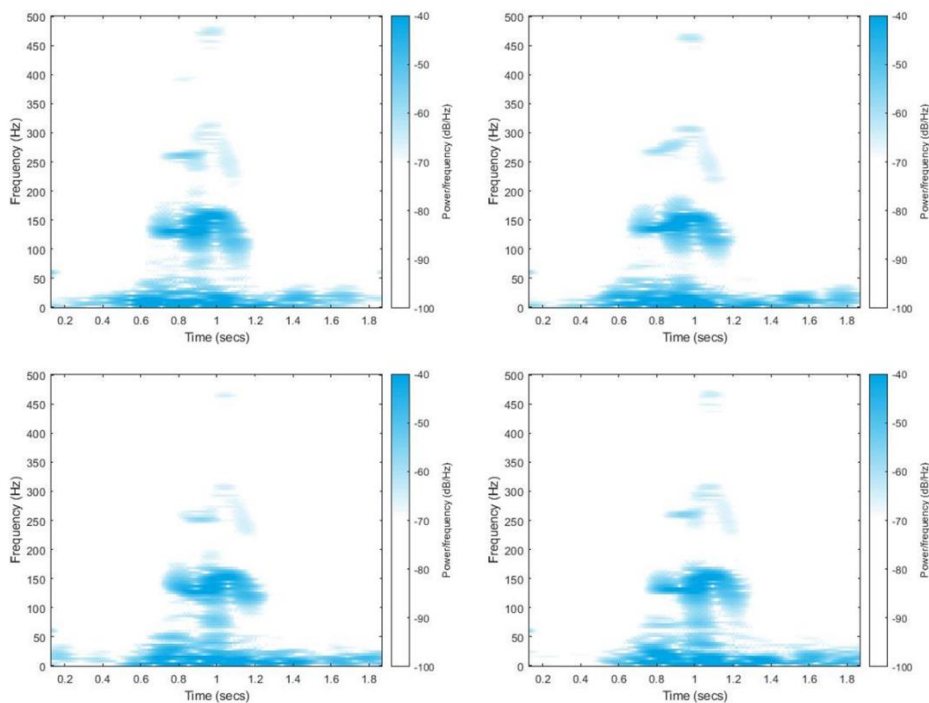


‘Up’:

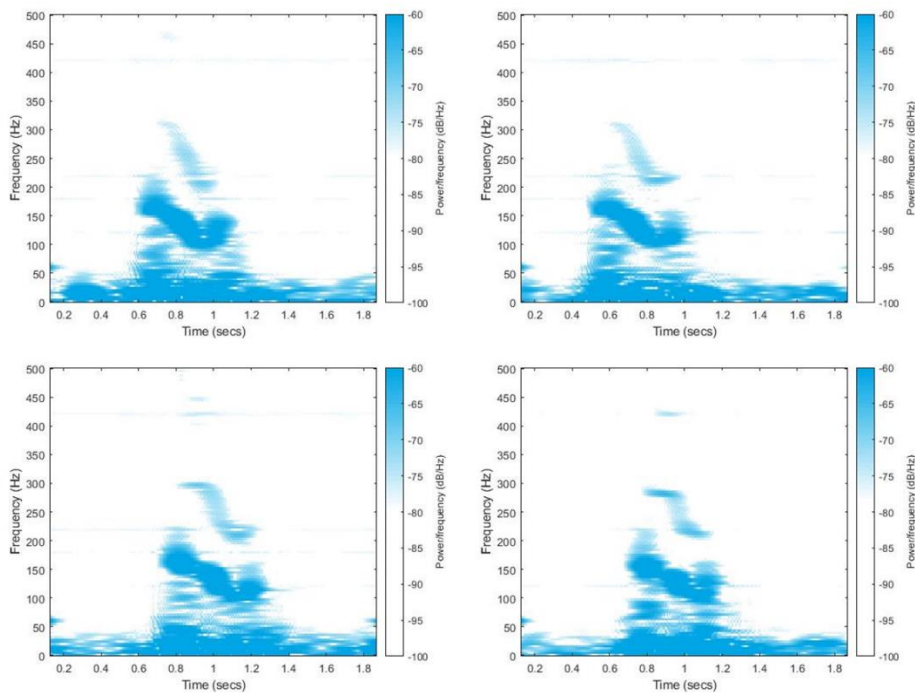


### A11: Voice spectrograms for speech recognition from PE bio-skin

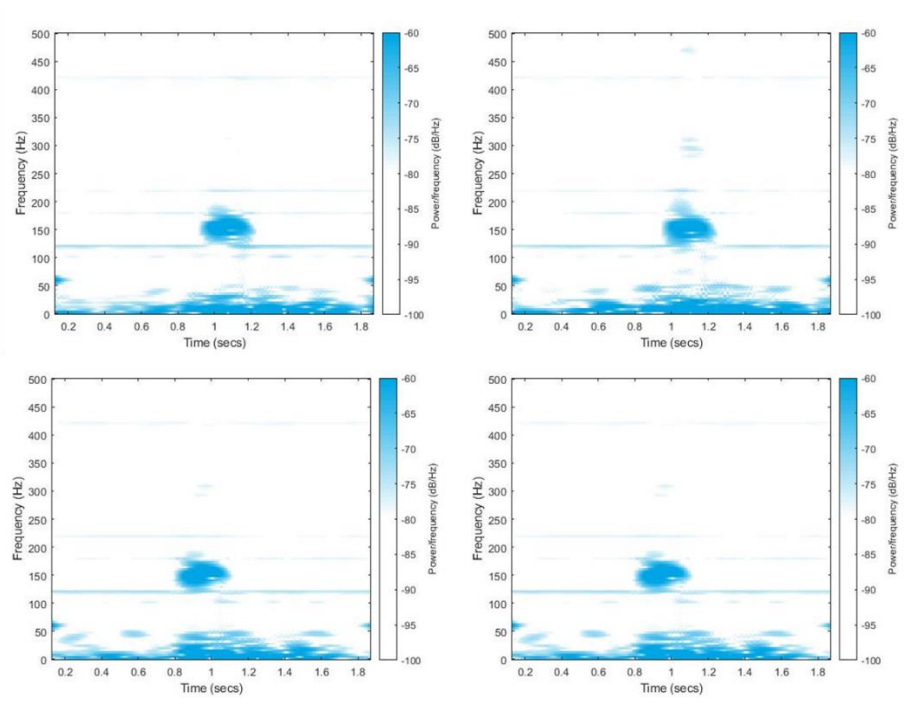
‘Purdue’:



‘Giant’:



‘Leaps’:



## REFERENCES

- [1] Lu X, McElroy MB, Kiviluoma J. Global potential for wind-generated electricity. *Proc Natl Acad Sci U S A*. 2009;106(27):10933-10938. doi:10.1073/pnas.0904101106
- [2] Scruggs J, Jacob P. Engineering. Harvesting ocean wave energy. *Science*. 2009;323(5918):1176-1178. doi:10.1126/science.1168245
- [3] Wang X, Song J, Liu J, Wang ZL. Direct-Current Nanogenerator Driven by Ultrasonic Waves. *Science (80- )*. 2007;316(5821):102-105. doi:10.1126/science.1139366
- [4] Wang S, Lin L, Wang ZL. Nanoscale Triboelectric-Effect-Enabled Energy Conversion for Sustainably Powering Portable Electronics. *Nano Lett*. 2012;12(12):6339-6346. doi:10.1021/nl303573d
- [5] Wang ZL, Song J. Piezoelectric nanogenerators based on zinc oxide nanowire arrays. *Science*. 2006;312(5771):242-246. doi:10.1126/science.1124005
- [6] Lin L, Wang S, Xie Y, et al. Segmentally Structured Disk Triboelectric Nanogenerator for Harvesting Rotational Mechanical Energy. *Nano Lett*. 2013;13(6):2916-2923. doi:10.1021/nl4013002
- [7] Zhang H, Yang Y, Su Y, et al. Triboelectric Nanogenerator for Harvesting Vibration Energy in Full Space and as Self-Powered Acceleration Sensor. *Adv Funct Mater*. 2014;24(10):1401-1407. doi:10.1002/adfm.201302453
- [8] Zhu G, Lin Z-H, Jing Q, et al. Toward Large-Scale Energy Harvesting by a Nanoparticle-Enhanced Triboelectric Nanogenerator. *Nano Lett*. 2013;13(2):847-853. doi:10.1021/nl4001053

- [9] Yang Y, Zhang H, Lin Z-H, et al. Human Skin Based Triboelectric Nanogenerators for Harvesting Biomechanical Energy and as Self-Powered Active Tactile Sensor System. *ACS Nano*. 2013;7(10):9213-9222. doi:10.1021/nn403838y
- [10] Yang R, Qin Y, Dai L, Wang ZL. Power generation with laterally packaged piezoelectric fine wires. *Nat Nanotechnol*. 2009;4(1):34-39. doi:10.1038/nnano.2008.314
- [11] Chen J, Zhu G, Yang W, et al. Harmonic-Resonator-Based Triboelectric Nanogenerator as a Sustainable Power Source and a Self-Powered Active Vibration Sensor. *Adv Mater*. 2013;25(42):6094-6099. doi:10.1002/adma.201302397
- [12] Lin L, Xie Y, Wang S, et al. Triboelectric Active Sensor Array for Self-Powered Static and Dynamic Pressure Detection and Tactile Imaging. *ACS Nano*. 2013;7(9):8266-8274. doi:10.1021/nn4037514
- [13] Fan F-R, Tian Z-Q, Lin Wang Z. Flexible triboelectric generator. *Nano Energy*. 2012;1(2):328-334. doi:10.1016/J.NANOEN.2012.01.004
- [14] Wang J, Li X, Zi Y, et al. A Flexible Fiber-Based Supercapacitor-Triboelectric-Nanogenerator Power System for Wearable Electronics. *Adv Mater*. 2015;27(33):4830-4836. doi:10.1002/adma.201501934
- [15] Pu X, Li L, Song H, et al. A Self-Charging Power Unit by Integration of a Textile Triboelectric Nanogenerator and a Flexible Lithium-Ion Battery for Wearable Electronics. *Adv Mater*. 2015;27(15):2472-2478. doi:10.1002/adma.201500311
- [16] Zhou R, Li J, Jiang H, et al. Highly transparent humidity sensor with thin cellulose acetate butyrate and hydrophobic AF1600X vapor permeating layers fabricated by screen printing. *Sensors Actuators B Chem*. 2019;281:212-220. doi:10.1016/J.SNB.2018.10.061
- [17] Li H, Zhao S, Du X, et al. A Compound Yarn Based Wearable Triboelectric Nanogenerator for Self-Powered Wearable Electronics. *Adv Mater Technol*. 2018;3(6):1800065. doi:10.1002/admt.201800065

- [18] Dong K, Wang Y-C, Deng J, et al. A Highly Stretchable and Washable All-Yarn-Based Self-Charging Knitting Power Textile Composed of Fiber Triboelectric Nanogenerators and Supercapacitors. *ACS Nano*. 2017;11(9):9490-9499. doi:10.1021/acsnano.7b05317
- [19] Wu, M., Wang, Y., Gao, S., Wang, R., Ma, C., & Tang, Z. et al. (2019). Solution-synthesized chiral piezoelectric selenium nanowires for wearable self-powered human-integrated monitoring. *Nano Energy*, 56, 693-699. doi: 10.1016/j.nanoen.2018.12.003
- [20] Huang, C., Song, J., Lee, W., Ding, Y., Gao, Z., & Hao, Y. et al. (2010). GaN Nanowire Arrays for High-Output Nanogenerators. *Journal Of The American Chemical Society*, 132(13), 4766-4771. doi: 10.1021/ja909863a
- [21] Lin, Y., Song, J., Ding, Y., Lu, S., & Wang, Z. (2008). Piezoelectric nanogenerator using CdS nanowires. *Applied Physics Letters*, 92(2), 022105. doi: 10.1063/1.2831901
- [22] Park, K., Xu, S., Liu, Y., Hwang, G., Kang, S., Wang, Z., & Lee, K. (2010). Piezoelectric BaTiO<sub>3</sub>Thin Film Nanogenerator on Plastic Substrates. *Nano Letters*, 10(12), 4939-4943. doi: 10.1021/nl102959k
- [23] Zhang, M., Gao, T., Wang, J., Liao, J., Qiu, Y., & Xue, H. et al. (2015). Single BaTiO<sub>3</sub> nanowires-polymer fiber based nanogenerator. *Nano Energy*, 11, 510-517. doi: 10.1016/j.nanoen.2014.11.028
- [24] Kudriavtsev, Aleksandr Andreevich. 1974. The chemistry & technology of selenium and tellurium. London: Collet's. <http://catalog.hathitrust.org/api/volumes/oclc/1257429.html>.
- [25] Liu, J., Xu, J., Liang, H., Wang, K., & Yu, S. (2012). Macroscale Ordered Ultrathin Telluride Nanowire Films, and Tellurium/Telluride Hetero-Nanowire Films. *Angewandte Chemie*, 124(30), 7538-7543. doi: 10.1002/ange.201201608
- [26] Wang, Y., Tang, Z., Podsiadlo, P., Elkasabi, Y., Lahann, J., & Kotov, N. (2006). Mirror-Like Photoconductive Layer-by-Layer Thin Films of Te Nanowires: The Fusion of Semiconductor, Metal, and Insulator Properties. *Advanced Materials*, 18(4), 518-522. doi: 10.1002/adma.200501465

- [27] Lee, T., Lee, S., Lee, E., Sohn, S., Lee, Y., & Lee, S. et al. (2013). High-Power Density Piezoelectric Energy Harvesting Using Radially Strained Ultrathin Trigonal Tellurium Nanowire Assembly. *Advanced Materials*, 25(21), 2920-2925. doi: 10.1002/adma.201300657
- [28] Wang, X. (2012). Piezoelectric nanogenerators—Harvesting ambient mechanical energy at the nanometer scale. *Nano Energy*, 1(1), 13-24. doi: 10.1016/j.nanoen.2011.09.001
- [29] Muth JT, Vogt DM, Truby RL, et al. Embedded 3D Printing of Strain Sensors within Highly Stretchable Elastomers. *Adv Mater*. 2014;26(36):6307-6312. doi:10.1002/adma.201400334
- [30] Skylar-Scott MA, Gunasekaran S, Lewis JA. Laser-assisted direct ink writing of planar and 3D metal architectures. *Proc Natl Acad Sci U S A*. 2016;113(22):6137-6142. doi:10.1073/pnas.1525131113
- [31] Amin R, Knowlton S, Hart A, et al. 3D-printed microfluidic devices. *Biofabrication*. 2016;8(2):022001. doi:10.1088/1758-5090/8/2/022001
- [32] Ilievski F, Mazzeo AD, Shepherd RF, Chen X, Whitesides GM. Soft Robotics for Chemists. *Angew Chemie*. 2011;123(8):1930-1935. doi:10.1002/ange.201006464
- [33] Gross BC, Erkal JL, Lockwood SY, Chen C, Spence DM. Evaluation of 3D Printing and Its Potential Impact on Biotechnology and the Chemical Sciences. *Anal Chem*. 2014;86(7):3240-3253. doi:10.1021/ac403397r
- [34] Vaezi M, Seitz H, Yang S. A review on 3D micro-additive manufacturing technologies. *Int J Adv Manuf Technol*. 2013;67(5-8):1721-1754. doi:10.1007/s00170-012-4605-2
- [35] Mueller B. Additive Manufacturing Technologies – Rapid Prototyping to Direct Digital Manufacturing. *Assem Autom*. 2012;32(2):aa.2012.03332baa.010. doi:10.1108/aa.2012.03332baa.010

- [36] Ventola CL. Medical Applications for 3D Printing: Current and Projected Uses. *P T*. 2014;39(10):704-711. <http://www.ncbi.nlm.nih.gov/pubmed/25336867>. Accessed November 27, 2018.
- [37] Rus D, Tolley MT. Design, fabrication and control of soft robots. *Nature*. 2015;521(7553):467-475. doi:10.1038/nature14543
- [38] Dua V, Surwade SP, Ammu S, et al. All-Organic Vapor Sensor Using Inkjet-Printed Reduced Graphene Oxide. *Angew Chemie Int Ed*. 2010;49(12):2154-2157. doi:10.1002/anie.200905089
- [39] Calvert† P. Inkjet Printing for Materials and Devices. 2001. doi:10.1021/CM0101632
- [40] Mata A, Kim EJ, Boehm CA, Fleischman AJ, Muschler GF, Roy S. A three-dimensional scaffold with precise micro-architecture and surface micro-textures. *Biomaterials*. 2009;30(27):4610-4617. doi:10.1016/J.BIOMATERIALS.2009.05.023
- [41] Bosi S, Rauti R, Laishram J, et al. From 2D to 3D: novel nanostructured scaffolds to investigate signalling in reconstructed neuronal networks. *Sci Rep*. 2015;5(1):9562. doi:10.1038/srep09562
- [42] Ozbolat V, Dey M, Ayan B, Povilianskas A, Demirel MC, Ozbolat IT. 3D Printing of PDMS Improves Its Mechanical and Cell Adhesion Properties. *ACS Biomater Sci Eng*. 2018;4(2):682-693. doi:10.1021/acsbomaterials.7b00646
- [43] Fan F-R, Lin L, Zhu G, Wu W, Zhang R, Wang ZL. Transparent Triboelectric Nanogenerators and Self-Powered Pressure Sensors Based on Micropatterned Plastic Films. *Nano Lett*. 2012;12(6):3109-3114. doi:10.1021/nl300988z
- [44] Lötters JC, Olthuis W, Veltink PH, Bergveld P. The mechanical properties of the rubber elastic polymer polydimethylsiloxane for sensor applications. *J Micromechanics Microengineering*. 1997;7(3):145-147. doi:10.1088/0960-1317/7/3/017

- [45] Hinton TJ, Hudson A, Pusch K, Lee A, Feinberg AW. 3D Printing PDMS Elastomer in a Hydrophilic Support Bath via Freeform Reversible Embedding. *ACS Biomater Sci Eng.* 2016;2(10):1781-1786. doi:10.1021/acsbiomaterials.6b00170
- [46] Patel DK, Sakhaei AH, Layani M, Zhang B, Ge Q, Magdassi S. Highly Stretchable and UV Curable Elastomers for Digital Light Processing Based 3D Printing. *Adv Mater.* 2017;29(15):1606000. doi:10.1002/adma.201606000
- [47] Fan, J., Yeo, W., Su, Y., Hattori, Y., Lee, W., & Jung, S. et al. (2014). Fractal design concepts for stretchable electronics. *Nature Communications*, 5(1). doi: 10.1038/ncomms4266
- [48] Furuta, N., Ohasi, Y., Itinose, H., & Igarashi, Y. (1975). Kinetics of Vapor-Grown Tellurium Whiskers. *Japanese Journal Of Applied Physics*, 14(7), 929-934. doi: 10.1143/jjap.14.929
- [49] Munn, R. (1994). *Molecular Electronics and Molecular Electronic Devices*. Kristof Sienicki (ed.). Volume 1, CRC Press, Boca Raton, FL, 1993, ISBN 0-8493-8061-9, 249 pp., £70.00 hardback. Volume 2, CRC Press, Boca Raton, FL, 1993, ISBN 0-8493-8062-6, 274 pp., £113.50 hardback. Volume 3, CRC Press, Boca Raton, FL, 1994, ISBN 0-8493-8063-4, 260 pp., £82.00 hardback. *Advanced Materials For Optics And Electronics*, 4(6), 431-432. doi: 10.1002/amo.860040608
- [50] Newton, R. (1972). *Tellurium*, W. Charles Cooper,(ed.), Van Nostrand Reinhold Co., New York(1971). 437 pages.\$22.50. *Aiche Journal*, 18(3), 670-670. doi: 10.1002/aic.690180341
- [51] Gao, S., Wang, Y., Wang, R., & Wu, W. (2017). Piezotronic effect in 1D van der Waals solid of elemental tellurium nanobelt for smart adaptive electronics. *Semiconductor Science And Technology*, 32(10), 104004. doi: 10.1088/1361-6641/aa8605
- [52] Wu, W., Wang, L., Yu, R., Liu, Y., Wei, S., Hone, J., & Wang, Z. (2016). Piezophototronic Effect in Single-Atomic-Layer MoS<sub>2</sub> for Strain-Gated Flexible Optoelectronics. *Advanced Materials*, 28(38), 8463-8468. doi: 10.1002/adma.201602854

- [53] Schwartz, G., Tee, B., Mei, J., Appleton, A., Kim, D., Wang, H., & Bao, Z. (2013). Flexible polymer transistors with high pressure sensitivity for application in electronic skin and health monitoring. *Nature Communications*, 4(1). doi: 10.1038/ncomms2832
- [54] Lin, Z., Chen, J., Li, X., Zhou, Z., Meng, K., & Wei, W. et al. (2017). Triboelectric Nanogenerator Enabled Body Sensor Network for Self-Powered Human Heart-Rate Monitoring. *ACS Nano*, 11(9), 8830-8837. doi: 10.1021/acsnano.7b02975
- [55] Chung, J., Lee, Y., Kim, J., Seong, M., Kim, S., & Lee, J. et al. (2010). Reference Values for the Augmentation Index and Pulse Pressure in Apparently Healthy Korean Subjects. *Korean Circulation Journal*, 40(4), 165. doi: 10.4070/kcj.2010.40.4.165
- [56] MILLASSEAU, S., KELLY, R., RITTER, J., & CHOWIENCZYK, P. (2002). Determination of age-related increases in large artery stiffness by digital pulse contour analysis. *Clinical Science*, 103(4), 371-377. doi: 10.1042/cs1030371
- [57] Digiglio, P., Li, R., Wang, W., & Pan, T. (2014). Microflotronic Arterial Tonometry for Continuous Wearable Non-Invasive Hemodynamic Monitoring. *Annals Of Biomedical Engineering*, 42(11), 2278-2288. doi: 10.1007/s10439-014-1037-1